JAMES | Journal of Advances in Modeling Earth Systems®

RESEARCH ARTICLE
10.1029/2023MS003855

Submesoscale-Permitting Physical/Biogeochemical Future Projections for the Main Hawaiian Islands

T. Friedrich[1,2], B. S. Powell[1], J. L. Gunnarson[1], G. Liu[1], S. F. Giardina[1], M. F. Stuecker[1,3], L. Hošeková[1], K. Feloy[1], and C. A. Stock[4]

[1]Department of Oceanography, University of Hawa'i at Mānoa, Honolulu, HI, USA, [2]Pacific Islands Ocean Observing System (PacIOOS), Honolulu, HI, USA, [3]International Pacific Research Center (IPRC), University of Hawai'i at Mānoa, Honolulu, HI, USA, [4]NOAA, Geophysical Fluid Dynamics Laboratory, Princeton, NJ, USA

Key Points:

- The first dynamically downscaled submesoscale permitting future climate projections for the main Hawaiian Islands are presented
- A careful treatment of global model output is critical to capture essential local oceanographic characteristics
- Hawai'i's near-surface ocean is likely to experience unprecedented acidification and substantial warming over the course of the century

Correspondence to:
T. Friedrich,
tobiasf@hawaii.edu

Citation:
Friedrich, T., Powell, B. S., Gunnarson, J. L., Liu, G., Giardina, S. F., Stuecker, M. F., et al. (2024). Submesoscale-permitting physical/biogeochemical future projections for the main Hawaiian Islands. *Journal of Advances in Modeling Earth Systems*, *16*, e2023MS003855. https://doi.org/10.1029/2023MS003855

Received 18 JUN 2023
Accepted 25 JAN 2024

Author Contributions:
Conceptualization: T. Friedrich, B. S. Powell, J. L. Gunnarson, G. Liu, S. F. Giardina, M. F. Stuecker, L. Hošeková, K. Feloy
Data curation: T. Friedrich, J. L. Gunnarson, S. F. Giardina
Formal analysis: T. Friedrich, J. L. Gunnarson, S. F. Giardina
Funding acquisition: T. Friedrich, B. S. Powell, M. F. Stuecker
Investigation: T. Friedrich
Methodology: T. Friedrich, B. S. Powell, J. L. Gunnarson, G. Liu, S. F. Giardina, M. F. Stuecker, L. Hošeková, K. Feloy
Project administration: T. Friedrich, B. S. Powell, M. F. Stuecker

Abstract Global climate models provide useful tools to forecast large-scale anthropogenic trends and the impacts on ocean physics and marine biology and chemistry. Due to coarse spatial resolution, they typically lack the ability to represent important regional processes while underestimating mesoscale variability and vertical mixing. This means they provide limited value when it comes to regional climate projections. We developed a regional submesoscale-permitting physical/biogeochemical model to dynamically downscale the output of a CMIP6 Earth System Model for three different Socioeconomic Pathways for the main Hawaiian Islands. We describe the methodology for downscaling the CMIP6 ocean physics and biogeochemistry along with atmospheric conditions in order to offline nest a regional model. We expect the large-scale spatial and temporal features of the global model to be retained by the regional model, while adding representation of the regional processes that are crucial to understanding climate change on a local scale. We compare the regional model representation against both observed data and a regional reanalysis over the first two decades of the century. We show that the regional model maintains the large-scale trends and interannual variability provided by the CMIP6 model while well-representing the regional dynamics that drive the short-term variability. To better illustrate the benefit of the downscaling, we present preliminary analysis of the downscaled results to examine climate impacts on the island corals that are not resolved by the global models. This analysis reveals that coastal corals are likely to experience unprecedented ocean acidification and substantial warming over the course of the century.

Plain Language Summary Climate models play an important role in projecting the changes in the ocean that may result from human-induced climate change; however, these models lack the ability to represent critical features important to regional localities. This means that high-resolution regional models are required to understand the impacts of climate change important to local communities. We describe how to downscale climate model solutions such that they can be used by high-resolution regional models to project local impacts of climate change. Our application is for the main Hawaiian Islands in the Pacific ocean that are highly dynamic but are missing from climate models. We also provide preliminary results of these projections that show regional impact on the island corals due to climate change.

1. Introduction

Recent projections carried out by the Coupled Model Intercomparison Project phase 6 (CMIP6) global climate models (Eyring et al., 2016) project potentially harmful changes to physical and biogeochemical ocean conditions in the North Pacific Subtropical Gyre (NPSG) (Kwiatkowski et al., 2020). Warming is leading to more severe ocean heat stress (Frölicher et al., 2018) as well as a stronger stratification of the upper water column. Increasing atmospheric CO_2 concentration is lowering the near-surface pH and the calcium carbonate saturation state (Kleypas et al., 1999; Orr et al., 2005). Data gathered by the Hawai'i Ocean Timeseries (HOT) program (Karl & Lukas, 1996) and at Station ALOHA (Karl & Church, 2018) to the north of the main Hawaiian Islands have documented these processes. These data reveal that from October 1988 to December 2020 sea surface temperature (SST) has increased by ~0.79°C, surface aragonite saturation has decreased by ~0.26, and pH has decreased by ~0.037 (Dore et al., 2009) (available from: https://hahana.soest.hawaii.edu/hot/hotco2/HOT_surface_CO2.txt; last visited on 9 November 2023).

Global Climate Model (GCM) projections are crucial when it comes to projecting the response to human-induced climate change, and CMIP6 represents the most current collaborative effort to conduct climate change

Resources: T. Friedrich, J. L. Gunnarson, M. F. Stuecker, C. A. Stock
Software: T. Friedrich, B. S. Powell, G. Liu
Supervision: T. Friedrich, B. S. Powell, M. F. Stuecker
Validation: T. Friedrich, J. L. Gunnarson, S. F. Giardina, L. Hošeková, K. Feloy, C. A. Stock
Visualization: T. Friedrich, B. S. Powell
Writing – original draft: T. Friedrich, B. S. Powell, J. L. Gunnarson, G. Liu, S. F. Giardina
Writing – review & editing: T. Friedrich, B. S. Powell, J. L. Gunnarson, G. Liu, S. F. Giardina, M. F. Stuecker, L. Hošeková, K. Feloy, C. A. Stock

simulations. These simulation results are most reliable when large spatial and long temporal scales are considered; however, relevant processes such as the impact of eddies on the larger-scale flow have to be parametrized. While these parameterizations do well at the global scale, they have been shown to be inadequate at regional-scales (Bahl et al., 2020; Lévy et al., 2018; McGillicuddy Jr, 2016). This has a feedback on the global scale and the underestimate of eddy mixing in GCMs has been shown to significantly underestimate primary productivity (Couespel et al., 2021). At smaller regional scales, global models lack the spatio–temporal resolution necessary to adequately represent critical small-scale dynamics such as eddy mixing, entrainment, and advection of biogeochemistry, frontal convergence and divergence, coastal processes, trapped waves, effects of tides, etc. These processes are absolutely essential to understanding regional physics and biogeochemistry, but more importantly, how these processes will potentially mitigate or enhance the large-scale signals imposed on the region by a changing climate. These processes will be crucial for understanding how and why some localized regions are refugia while others are not. Nesting regional ocean models in GCMs has emerged as a necessary tool to dynamically downscale results to examine dominant regional processes and features as shown in the California Current System (Gruber et al., 2012; Hauri et al., 2013; Siedlecki, Pilcher, et al., 2021), the Bering Sea (Pilcher et al., 2022), the Gulf of Maine (Siedlecki, Salisbury, et al., 2021), the Canadian Pacific continental margin (Holdsworth et al., 2021), and others. Please see Drenkard et al. (2021) for a comprehensive overview.

In this study, we extend these dynamical climate-change downscaling efforts to the waters around the main Hawaiian Islands (MHI). The MHI encompass the eight easternmost islands of the Hawaiian–Emperor seamount chain (Ni'ihau, Kaua'i, O'ahu, Moloka'i, Lana'i, Maui, Kaho'olawe, and Hawai'i, Figure 1). The MHI have a strong gradient in biological abundance from oligotrophic waters over the abyssal plain to biologically diverse coral reef ecosystems surrounding the islands. This biodiversity is critical to the islands from the commercial fishing of pelagic tuna and swordfish to the coral reefs that provide coastal protection, marine life sustenance, and are an important component of cultural values.

Hawai'i sits on the southern portion of the return flow of the NPSG and the permanent thermocline of the NPSG creates an oligotrophic regime (Karl & Church, 2017). The Hawaiian archipelago exerts significant influence on the climate of the North Pacific ocean (Xie et al., 2001). The Hawaiian Islands are steep mountains rising from the abyssal floor to over 4 km above sea-level. They disrupt both the north-east trade winds and the westward flowing North Equatorial Current (NEC, Figure 1). The trade-wind driven NEC impinges upon the Hawaiian Islands at lower latitudes resulting in the northwestward flowing North Hawaiian Ridge Current (NHRC) to the north of the islands and a westward continuation of the NEC in the southern part of the domain (Lumpkin & Flament, 2013).

Strong winds forced between the islands result in regions of increased wind-stress curl in the lee of the islands (Chavanne et al., 2002). Further west, these winds coalesce to form a wake that extends for 3,000 km behind the islands (Xie et al., 2001). These wind-stress patterns drive the eastward Hawaii Lee Countercurrent (HLCC) west of the island of Hawai'i that is redirected to the north as the Hawaii Lee Current (HLC) on the southern side of the islands (Figure 1). The strong shear zone between the NEC and the HLCC (Qiu & Durland, 2002; Xie et al., 2001) makes the Hawaiian Islands a strong driver for mesoscale and submesoscale activities. In the lee of the islands, strong cyclonic and anticyclonic eddies are formed (Calil et al., 2008; Nencioli et al., 2008). Further west of the islands, the lateral shear between the NEC and HLCC drives baroclinic instabilities that form anticyclonic eddies at a regular frequency (Yoshida et al., 2010). Cyclonic eddies have been shown to have a strong effect on nutrient availability, productivity and ecosystem composition in this region (Brown et al., 2008; Friedrich et al., 2021; Nencioli et al., 2008; Rii et al., 2008). By comparison, anticyclonic eddies can increase the abundance of N_2-fixing microorganisms (Böttjer et al., 2017; Church et al., 2009). Furthermore, the straining of water masses that occurs on the fronts of eddies can result in a spin up of a vertical circulation cells (Calil & Richards, 2010; Mahadevan, 2016) which can also affect primary productivity and marine carbon cycle by acting on vertical nutrient and carbon gradients.

In addition to vertical displacement in the core of eddies and mixing along their fronts, internal waves drive substantial displacement and mixing around the islands. The Hawaiian archipelago is an important site of barotropic tidal dissipation with estimates of 2.7 GW just along the Ka'ena Ridge from M_2 alone (Carter et al., 2008). This dissipation is due to the ridges of the archipelago situated orthogonally to the propagation of the M_2 that results in pronounced semidiurnal baroclinic tides radiating from the ridges (Carter et al., 2008; Dushaw et al., 1995; Ray & Mitchum, 1996, 1997). The dissipation of tidal energy is a regular process and can induce horizontal and vertical transport of biogeochemical tracers (Jan & Chen, 2009; Macías et al., 2007).

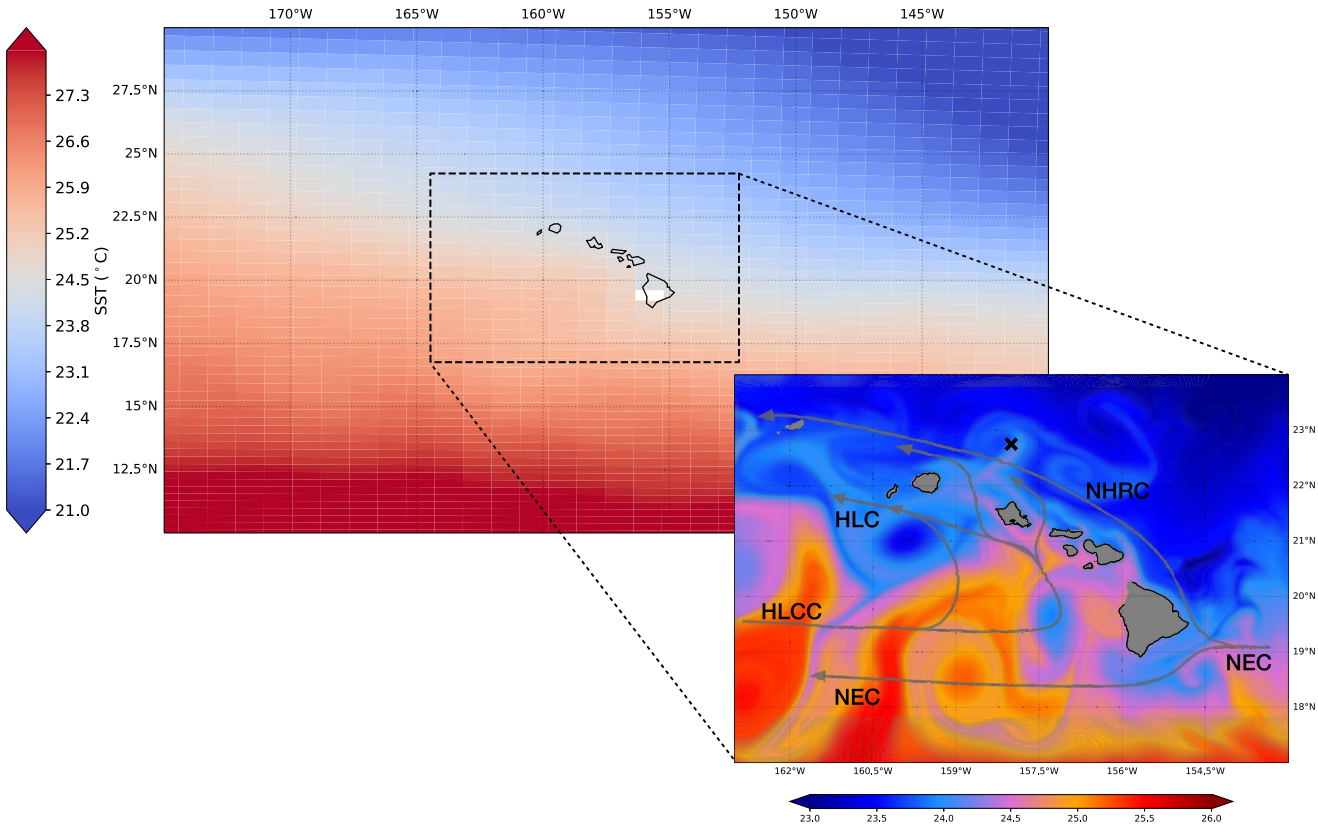

Figure 1. Domain of regional ROMS/COBALT model (dashed rectangular). A snapshot of monthly mean SST (°C) is shown for CESM2 (upper panel) and ROMS/COBALT (inlay) to illustrate the location of the model domain as well as different horizontal model resolutions. CESM2 does not represent the islands of Hawai'i, merely one rectangular island. The cross indicates the location of Station ALOHA. Arrows indicate a schematic map of the mean currents around Hawai'i. Please see text for details.

All of these processes create a dynamically diverse region with scales varying from planetary (NEC) to sub-mesoscale fronts around the islands that drive substantial natural variability of physical and biogeochemical ocean conditions that can vary differently from the larger-scale climate trends. Fine-scale vertical transport locally alters the large-scale trend toward increasing stratification (Couespel et al., 2021) mitigating the effects regionally. Coarse-resolution GCMs are incapable of resolving or parameterizing these processes. Understanding the complexities of the spatial gradients in biodiversity as well as the range of dynamical processes around Hawai'i (from winds and ocean circulation to coastal and pelagic ecosystem dynamics and connectivity) requires a regional model of high spatial and temporal resolution.

While regional models nested within GCMs provide the necessary resolution to capture the processes, they must maintain balance with the large-scale flow (planetary Sverdrup flows, mean currents, etc.), long-time variability (annual cycle, inter-annual variability, decadal variability), and trends (climate warming, acidification, deoxygenation, etc.).

In this paper, we present the methods required to offline nest a previously developed, high-resolution regional physical/biogeochemical model (Friedrich et al., 2021) of Hawai'i within a GCM. We will nest within CMIP6 CESM2 model output of differing emission scenarios. We have previously shown (Friedrich et al., 2021) that this regional model has skill at resolving all of the dominant processes described: the model represents the eddy effects on the physics (Souza et al., 2015) and biogeochemistry as compared to the observed biology (Brown et al., 2008; Nencioli et al., 2008; Rii et al., 2008); it captures the effects of eddies on coral reef connectivity (Wong-Ala et al., 2018) and fish aggregation (Leitner et al., 2021); it well captures the spatial extend of the island mass effect (Gove et al., 2016) as compared to satellite chlorophyll; and, it captures the internal tide generation and propagation (Powell et al., 2012).

We have three expectations with this paper. First, we develop a dynamical downscaling effort to resolve processes critically important to physical and biogeochemical dynamics in our domain. Second, as described above, we must ensure that the downscaling method allows for regional dynamics to evolve while maintaining parity with the large-scale variability and trends. Finally, with successful results of the first two, we aim to provide a preliminary analysis of the downscaled results to examine climate impacts on the island corals that are not resolved by the global models.

This paper serves as the methodology and validation of the downscaling method and its application to a regional model of Hawai'i, and it will serve as the basis for other scientific studies aimed at identifying the importance and evolution of regional Hawaiian processes in the context of large-scale anthropogenic climate change. The downscaled model is intended to ultimately provide robust, high-resolution projections of changing ocean physics, biological productivity, and carbonate chemistry conditions for Hawaiian waters.

2. Methods

We have developed a methodology to downscale forcing from five separate CMIP6 projections from 2000 to 2100 using three different Shared Socioeconomic Pathways (SSP) scenarios. In all cases, the Community Earth System Model version 2 (CESM2) is used as the GCM. We use the CESM2 atmospheric, oceanic, and biogeochemical fields (with some caveats below) around the MHI (see Figure 1) to force our regional model. The regional model is based on the Regional Ocean Modeling System (ROMS) online coupled with the Carbon, Ocean Biogeochemistry and Lower Trophics (COBALT) ecosystem model as described in Friedrich et al. (2021).

2.1. Global Model

The CESM2 is a state-of-the-art, coupled Earth system model with active biogeochemistry (Danabasoglu et al., 2020). The model incorporates the Community Atmosphere Model version 6 and Parallel Ocean Program version 2 ocean model, both on ∼1° horizontal grids, as well as coupled land, sea ice, wave, marine biogeochemical, and river runoff models. The CESM2 large ensemble (LE) consists of 100 ensemble members covering the period 1850–2100 using CMIP6 historical and Shared Socioeconomic Pathways (SSP) 3–7.0 forcing protocols (Rodgers et al., 2021). The SSP3–-7.0 scenario, which has a high level of emissions (O'Neill et al., 2016), was chosen to investigate forced changes in climate variability. Two different methods were used to initialize the CESM2-LE ensemble members. Four groups of 20 ensemble members were initialized at different years of the CESM2 preindustrial control simulation corresponding to different states of the Atlantic meridional overturning circulation. Within each group of 20, the ensemble spread was created by introducing small, random atmospheric temperature perturbations. Another group of 20 members was initialized from different years of the control simulation (at 10-year intervals from years 1001 to 1091). Fifty ensemble members were run with a smoothed biomass burning modification to the CMIP6 historical forcing.

For this regional downscaling effort, we chose three ensemble members to downscale for the MHI region using several criteria to ensure different realizations of internal climate variability. We chose the first ensemble member to most closely match the observed temporal standard deviation of area-averaged monthly SST anomalies ($\sigma(SST_{\mathrm{obs}})$) and June-July-August trade wind strength anomalies ($\sigma(U_{\mathrm{obs}})$, represented by the wind speed magnitude at the 10-m level, $|U_{10}|$) in the ERA5 reanalysis (Hersbach et al., 2020) over the time period 1979–2020 in a rectangle surrounding the MHI (Figure 1). We normalized the SST and $|U_{10}|$ standard deviations for each ensemble member ($\sigma(SST_i)$, $\sigma(U_i)$) by subtracting the observed standard deviations and then dividing by the ensemble mean standard deviations for each variable ($\langle\sigma(SST)\rangle$, $\langle\sigma(U)\rangle$) and calculated the total deviation for each ensemble member (Δ_i) as the sum of the two weighted differences:

$$\Delta_i = \sqrt{\left(\frac{\sigma(SST_i) - \sigma(SST_{\mathrm{obs}})}{\langle\sigma(SST)\rangle}\right)^2 + \left(\frac{\sigma(U_i) - \sigma(U_{\mathrm{obs}})}{\langle\sigma(U)\rangle}\right)^2} \quad (1)$$

Member LE2–1301.009 exhibits the smallest deviation from the observational records and was selected as the first simulation.

The other two members were selected based on their SST anomaly variance in the Niño3.4 region. The El Niño Southern Oscillation (ENSO) has numerous effects on atmospheric and ocean conditions in our domain. Most

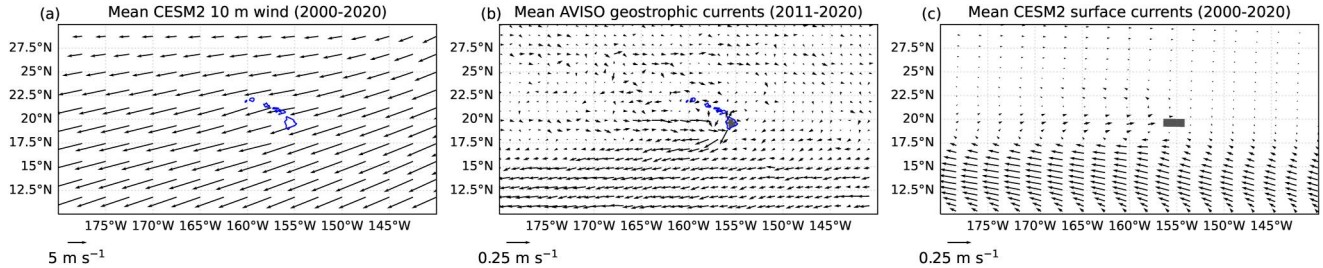

Figure 2. (a) Mean (2000–2020, LE2–1301.009) CESM2 10 m wind (m s^{-1}). (b) Mean (2011–2020) AVISO geostrophic currents (m s^{-1}). (c) Mean (2000–2020, LE2–1301.009) CESM2 surface currents in m s^{-1}. Every second (fourth) vector is shown for CESM2 (AVISO) for clarity.

relevant for our simulations are arguably the impacts on winds and temperatures. Trade winds typically weaken during El Niño conditions resulting in decreased momentum transfer to the surface ocean as well as reduced wind shear around the islands which has the potential to affect ocean currents and eddy generation. Furthermore, latent heat fluxes are reduced. ENSO related SST anomalies (September–February) are generally characterized by a dipole pattern across our domain (Webb & Magi, 2022) with warmer-than-normal SSTs in the south-eastern part during El Niño conditions. As a consequence, in "quiet ENSO" periods, we can expect weaker impacts on SSTs and winds in Hawaiian waters, whereas during "active ENSO" periods we expect stronger effects. Accordingly, we selected ensemble members with the highest (member LE2–1231.003) and lowest (member LE2–1231.010) Niño3.4 SST anomaly variances respectively, representing the high and low extremes of ENSO-related tropical climate variability in the CESM2-LE during this time period. The warming related ensemble-mean ENSO SST variance peaks during the decades 2041–2070 for the CESM2 Large Ensemble (see Figure 4 in Maher et al. (2022)). Hence, this period is used as a reference to select the members that have maximum and minimum variance at the peak of the ensemble-mean Niño3.4 variance representing the highest ENSO variance possible in the entire run of the model.

In addition to the three SSP3–7.0 ensemble members, two other SSP scenarios were investigated and modeled to evaluate the overall range of potential climate change. Output from a low-emission (SSP1–2.6) and a moderate-emission (SSP2–4.5) CESM2 simulation were downloaded from the CMIP6 archive to derive boundary conditions and forcing for our regional projections. It should be noted that although it would have been desirable to utilize more ensemble members for the lower emission scenarios, it would have been computationally too costly to conduct more than five one hundred year long simulations.

Once the climate scenarios and data were selected, the first step before beginning the downscaling was to ensure that the CESM2 simulations resolved the large-scale processes that are crucial to the MHI region. As discussed earlier, the MHI create a pronounced disruption to the climate of the subtropical Pacific. For our regional model to simulate these dynamics, the global model needs to capture the large-scale patterns that are disrupted. This requires that the north-easterly trade-winds are well represented in the global model. As can be seen in Figure 2a, the time-averaged (2000–2020) winds simulated by CESM2 around the MHI are dominated by a north-easterly direction with wind speeds of 5–8 m s^{-1}. CESM2 represents the MHI with a single island mass that only reaches a maximum elevation of ∼200 m. For comparison, the two mountains of the island of Hawai'i have elevations of 4,207 and 4,169 m, and the mountain on the island of Maui reaches 3,055 m in height. This means that the wind field of CESM2 represents winds across an open ocean rather than around the islands.

As the MHI lie in the southern extent of the NPSG, another requirement is that the location and strength of the NPSG is represented, particularly with the NEC that is obstructed by the MHI. In addition, the sub- to tropical Pacific contains a number of flows and counter flows as part of the planetary circulation (Qiu & Chen, 2010; Qiu et al., 2013). The most important of these for the Hawaiian domain are the NEC and the HLCC that brings warm waters from the Philippine Sea to Hawai'i (Figure 2b) (Lumpkin & Flament, 2013; Qiu & Durland, 2002). While the strength and variability of the representation of these large-scale flows may vary between projections, both of these currents are represented by each of the CESM2 projections selected (Figure 2c). The flows are shifted slightly equatorward as compared to observed patterns; however, the overall flow patterns in strength and direction are represented by CESM2.

Table 1
Overview of ENSO Events Based on the Oceanic Niño Index (ONI) for the NOAA SST Record and the Community Earth System Model 2 (CESM2) Simulations Used for Our Regional Projections

SST data	1935–2020		2015–2100	
Source	Strong/very strong (ONI > 1.5°C)	Weak/moderate (0.5° C < ONI ≤ 1.5°C)	Strong/very strong (ONI > 1.5°C)	Weak/moderate (0.5° C < ONI ≤ 1.5°C)
NOAA	10	12	N.A.	N.A.
LE2–1301.009	15	10	20	15
LE2–1231.003	15	9	22	7
LE2–1231.010	13	12	16	11
CMIP6-historical.011/CMIP6-SSP2–4.5.102	16	7	23	8
CMIP6-historical.011/CMIP6-SSP1–2.6.102	16	8	17	10

In addition to the large-scale mean currents, we expect that the CESM2 projections well represent the interannual climate variability of the Pacific, particularly the dominant ENSO signal. We examine the CESM2 projections by comparing the Oceanic Niño Index (ONI; Glantz & Ramirez, 2020) to determine El Niño events over the past 85 years and compare to the next 85 years. Following the National Center for Atmospheric Research, El Niño events are classified by an ONI value of 0.5°C or higher for five consecutive 3-month running means (Glantz & Ramirez, 2020) with weak/moderate events being characterized by an ONI between 0.5 and 1.5°C whereas an ONI > 1.5°C indicates strong/very strong events. We compare the past century for each CESM2 integration with the NOAA SST product.

Since the climate fluctuations in the historical period of a climate change projection are not expected to coincide with the timing of observed fluctuations, we focus on the number and strength of ENSO events over a common period.

We examined the historical period from 1935 to 2020 calculating ONI from the CESM2 projections and the NOAA SST (Huang et al., 2017). NOAA SST derived ONI reveals 10 strong/very strong (S/VS) events and 12 weak/moderate (W/M) events occurred (Table 1). The CESM2 projections were consistent, revealing 13–16 S/VS events and 7–12 W/M events. This suggests that the models have a similar frequency and strength of ENSO variability as observed.

These calculations were also done for the future time period (2015–2100) of all simulations (Table 1). The 3 SSP3–7.0 runs had an average of 19 S/VS events, and 11 W/M events. The SSP2–4.5 run had 23 S/VS events, and 8 W/M events, and the SSP1–2.6 run had 17 S/VS events and 10 W/M events. For the 3 SSP3–7.0 runs, there was an overall increase of 22.97% in total events. In the SSP2–4.5 (SSP1–2.6) run, this increase amounts to 34.78% (12.50%).

An analysis of spatial patterns of the El Niño events was also performed to describe Eastern Pacific (EP) and Central Pacific (CP) events. Determinations were done using the three methods described in Yu et al. (2012); EP/CP method, Niño3/4 Method, and EMI method. The Trans-Niño index was also used as an additional metric for determining EP/CP events. For the past period, the division was in the order of 40%–50% EP and 50%–60% CP depending on the model simulation. For the future, the division is projected to be 36% EP and 64% CP for the 3 SSP3–7.0 runs and 40% EP and 60% CP for the other two scenarios. More details on the representation of ENSO in CESM2 and as well as the simulated ENSO teleconnections can be found in Danabasoglu et al. (2020).

These results give us confidence that the CESM2 simulations provide a good representation of the planetary signals required to force a regional simulation of the MHI. We now turn to comparing general outcomes from each of the CESM2 projection. Table 2 provides an overview of surface temperature and pH changes for the different CESM2 simulations utilized in the study. The SSP3–7.0 scenarios result in a simulated global 2 m air temperature increase of 3.88–4.04°C over the course of the 21st century and an associated global SST increase of 2.06–2.11°C. The corresponding values for the SSP2–4.5 and SSP1–2.6 scenarios are 2.84 and 1.78°C (2 m air temperature) and 1.55 and 1.00°C (SST), respectively. SST changes for our model domain range from 1.64°C (SSP1–2.6) to

Table 2
Overview of Surface Warming and Ocean Acidification in the CESM2 Simulations Used for Our Regional Projections

Name in CMIP6 archive	SSP scenario	21st century global 2 m air temperature change (°C)	21st century global SST change (°C)	21st century SST change for Hawai'i domain (°C)	21st century surface pH change for Hawai'i domain
LE2–1301.009	3–7.0	3.88	2.06	3.13	−0.33
LE2–1231.003	3–7.0	4.04	2.11	3.25	−0.33
LE2–1231.010	3–7.0	3.94	2.10	2.80	−0.33
CMIP6-historical.011/ CMIP6-SSP2–4.5.102	2–4.5	2.84	1.55	2.23	−0.20
CMIP6-historical.011/ CMIP6-SSP1–2.6.102	1–2.6	1.78	1.00	1.64	−0.08

Note. The 21st century change is based on the quadratic slope of a least-square fit of monthly mean surface data.

3.13°C (highest SSP3–7.0 run). It is noteworthy that the spread between the different SSP3–7.0 simulations is on the same order of magnitude as the difference between the lowest SSP3–7.0 run and the SSP2–4.5 simulation. The pH decrease simulated by CESM2 for our regional domain amounts to −0.33 for the SSP3–7.0 scenario. For the lowest GHG emission scenario, a maximum decrease of −0.1 is reached around year 2067 followed by a recovery, resulting in an overall decrease of −0.08 at the end of the century.

2.2. Regional Model

To model the evolution of ocean physics and biogeochemistry around the MHI over the course of the 21st century we use the ROMS coupled to the planktonic COBALT ecosystem model. ROMS is a free surface, hydrostatic, primitive equation model using a terrain-following, stretched coordinate system in the vertical. ROMS utilizes a split-explicit time stepping scheme to allow different time steps for the barotropic and baroclinic components (Shchepetkin & McWilliams, 1998, 2003, 2005).

The model domain includes the MHI (Figure 1, inlay) with bathymetry data provided by the Hawaiian Mapping Research Group (HMRG, 2017). The grid has 4 km horizontal resolution with 32 vertical s-levels, configured to provide a higher vertical resolution in the more variable upper regions. More details of the grid configuration of the model, including the vertical stretching scheme, is presented in Souza et al. (2015) and Partridge et al. (2019). A sponge region of 12 grid cells (48 km) along each of the four open boundaries linearly increases the viscosity by a factor of four and diffusivity by a factor of two at the boundary to account for imbalances between lateral boundary conditions and ROMS. Lateral boundary conditions for ocean physics are taken from monthly mean data from CMIP6 scenarios using CESM2.

The simulations are run with tidal forcing using the Oregon State University Tidal Prediction Software (Egbert et al., 1994). The tidal constituents included are the eight main harmonics; M_2, S_2, N_2, K_2, K_1, O_1, P_1, Q_1, as well as two long period and one non-linear constituent; M_f, M_m, and M_4. The tidal harmonics are updated each year of the simulation to define the phases referenced to the middle of that year in order to avoid any long term drifting of the tidal amplitudes and phases related to constituents that are not considered. Riverine output is not prescribed in this model as the Hawaiian Islands lack any major river system. While there is regular outflow from numerous streams into the coastal environment that contains various nutrients, these average under 100 $m^3\ s^{-1}$. As a result, the streams dissipate in the near-shore and wave-breaking environment and are not an important influence on the coastal and open ocean waters.

The ROMS model is online coupled to the COBALT model (Stock et al., 2014) integrated into the same codebase. This ROMS/COBALT has been successfully developed and configured for the MHI (Friedrich et al., 2021). The results showed that ROMS/COBALT exhibits good agreement between simulated values and observations at Station ALOHA (Karl & Church, 2018). COBALT uses 33 state variables to resolve cycles of carbon, nitrogen, phosphorous, iron, and silica. Nitrogen serves as the biomass currency variable and is combined with carbon based on the Redfield ratio of 106:16 (Redfield, 1963). COBALT simulates three phytoplankton groups: small, large, and diazotrophs as well as small (<200 μm), medium (200–2,000 μm), and large (2–20 mm) zooplankton. Oxygen and carbon are exchanged between the atmosphere and the ocean using prescribed atmospheric

concentrations of the two gases. Total alkalinity (TA) and dissolved inorganic carbon (DIC) are used as tracers for the marine carbon cycle. Model dynamics, parameters, and equations are presented in full detail in Stock et al. (2014).

Compared to the configuration outlined in Friedrich et al. (2021), several updates have been made:

- COBALT code was updated to the latest version of ROMS v4.1 from October 2022.
- Modifications were made to the code to allow separate time-stepping. COBALT ecosystem dynamics are now integrated with a time step of 3,600 s and the ROMS time step remains at 400 s (which includes advection and diffusion of COBALT tracers). Thorough testing revealed that a 1-hr time step yields virtually identical results for all biogeochemical fields while saving about 25% of computation time.
- Previous tests showed that the modeled light propagation through the water column did not match the observations at Station Aloha. We modified the parameters for the light attenuation scheme (Manizza et al., 2005) by fitting the modeled light output to the observed light and radiance data collected from the HOT program. The blue parameters (k_{sw} and ξ) were changed from 0.0232 m^{-1} and 0.074 m^{-2} mgChl m^{-3}, respectively, to 0.009 m^{-1} and 0.062 m^{-2} mgChl m^{-3}. This produces an attenuation that matches the long-term data of HOT resulting in more blue light energy at deeper layers of the euphotic zone. This additional blue light leads to a ∼20–40 m deeper chlorophyll maximum layer (depending on the season) as compared to the results of Friedrich et al. (2021). This deeper chlorophyll maximum layer provides a better representation of chlorophyll as compared to the HOT at the Station ALOHA location. As the waters around the MHI are deep abyssal ocean waters, this change to the light scheme should be optimal for the region.
- Surface freshwater fluxes are now considered in the surface budgets of DIC and TA (dissolution and concentration). The simulated domain-average salinity–alkalinity relationship at the surface has a slope of 66.5 μmol kg^{-1} per psu which is in good agreement with the one found for monthly HOT data (Dore et al., 2009): 66.2 μmol kg^{-1} per psu.

2.3. Downscaling

Much of the difficulty in running nested regional models within larger GCMs is how to properly force the regional model so that it remains consistent with the GCM on the large-scale, is free to develop regional dynamics, remains in balance between the atmosphere, ocean, and ecosystem, and does not introduce significant aliasing or other noise to the system.

2.3.1. Atmospheric Forcing

The initial step for any downscaling ocean system is to first capture the balance between the GCM atmosphere and ocean. Evolving regional differences in oceanic flow results in imbalances between prescribed heat fluxes and other properties that can lead to energy and mass imbalances. As such, special care must be given to ensure that the heat, salt, and momentum balance between the atmosphere and ocean is maintained without compromising the ability of the downscaled oceanic flow to evolve. Atmospheric forcing fields required by ROMS/COBALT using bulk fluxes (Fairall et al., 1996) are: sea-level pressure in hPa, relative humidity in percentage, downwelled long- and shortwave radiation in W m^{-2}, 2 m air temperature in °C, rainfall in kg m^{-2} s^{-1}, 10 m winds in m s^{-1}, atmospheric pCO_2 in ppmv, atmospheric iron flux (mol m^{-2} s^{-1}). ROMS performs online temporal and spatial interpolation of atmospheric forcing fields to the ROMS grid, so we may specify these constituents at the available resolutions.

Several of the forcing fields can be used with minimal effort from CESM2. Fields with large-scale spatial gradients that are captured well by the coarse GCM can be used with minor modification. Surface air pressure, relative humidity, shortwave and longwave radiation are taken directly from daily mean CESM2 output. The daily mean of downwelled shortwave radiation forcing is converted online by ROMS based on latitude and season to impose a diurnal cycle in light for modeling biological productivity. After testing different values and comparing the downscaled SSTs to CESM2 and HOT observations, we reduced the downwelled longwave radiation by 30% to account for energetic imbalances between CESM2 and ROMS. The atmospheric pCO_2 concentrations are taken from CESM2 monthly average. Atmospheric iron input is based on an estimate by Letelier et al. (2019) and set to 7.3 μmol m^{-2} yr^{-1}.

The remaining atmospheric forcing fields (2 m air temperature, rainfall, and 10 m winds) are not well represented by CESM2 due to the short temporal and spatial scales that result due to interactions with the mountains of the MHI. These crucially important dynamics around the islands are a dominant forcing in the ocean circulation of the MHI, and it is a requirement that these processes are captured. This requires us to treat these fields differently and use an atmospheric model that reproduces the fine-scale structure of the MHI. As used in Friedrich et al. (2021), we employ high-resolution hindcast output of a regional Weather Regional Forecast (WRF) model configured for the MHI (Chen, 2010). This daily operational WRF product is part of the Pacific Islands Ocean Observing System and is nested within the National Center for Environmental Prediction Global Forecasting System using 3D-Var to assimilate regional data (Tu et al., 2017; Zho & Chen, 2014). The WRF model has been shown to well represent the small-scale atmospheric circulation around the MHI (Hitzl et al., 2014, 2020; Stopa et al., 2013). WRF data are available publicly (http://www.pacioos.hawaii.edu). We use 10 years of three-hourly output from the WRF model for the period 2010–2020 to generate the basis for each of the remaining forcing fields.

For rainfall, there is no observable trend in rainfall around the MHI from the CESM2 results for the MHI for the 21st century, so we use a 10-year 3-hourly climatology of rainfall from WRF. The primary effect of rain on the ocean simulation is the dilution of surface carbonate variables.

The 2 m air temperature as shown by the 10 years WRF for the MHI exhibits a strong spatial structure with short-scale variability in the lee of the islands and other regions; however, the CESM2 simulations cannot resolve these variations. Over the century, the CESM2 does represent large-scale interannual and longer variability along with a warming trend over the period.

In order to capture both the large-scale temperature variability and trend in addition to the regional structure, we utilize a three-hourly WRF climatology (calculated for all three-hourly fields over 10 years) that is scaled to include the temporal (interannual, decadal, warming, etc.) trends represented by CESM2. We follow these steps to combine the WRF spatial climatology with temporal variations from CESM2: (a) we convert our WRF climatology into 2 m air temperature anomalies by removing the monthly domain-wide mean from the three-hourly WRF 2 m air temperature climatology (Figure 3a); (b) we calculate the domain-wide monthly mean from the CESM2 data (Figure 3b); (c) the monthly mean values are linearly interpolated in time and added to the three-hourly WRF anomaly fields. This ensures that we have temperatures that represent the spatial structure of the MHI (albeit, we do not have short-term spatial variability in 2 m air temperature due to storms, etc.) but that maintains—in the mean—the heat balance of CESM2 while following the CESM2 seasons, interannual and longer variability, as well as any trends.

As described in Section 1, the dominant wind forcing of the MHI domain is provided by the wind shear created by the impingement of tall mountains into the atmospheric flow that drives genesis of mesoscale and submesoscale features around the islands. This wind shear cannot be resolved by CESM2 (Figures 3c and 3d). To address this issue, we developed a novel neural network approach to downscale the patterns of winds from CESM2 (Liu et al., 2023). A brief explanatory summary is that we calculated the long-term Empirical Othogonal Functions (EOFs) of the wind structures from the 2010–2020 period of the WRF results. The first 10 EOF modes explain 95% of the wind variability and are used. Comparison between the dominant EOF modes from CESM2 winds show a strong correspondence between WRF and CESM2 for the prevalent trade-wind structure. A Convolution Neural Network (CNN) (Höhlein et al., 2020) was then trained to predict the principal components of the ten WRF-based EOF modes when provided the CESM2 winds as input. The CNN identifies the large-scale structure given by the CESM2 output and provides the necessary principal components to reconstruct the fine-scale WRF field that best represents the MHI wind field when forced by the large-scale winds. As presented in Liu et al. (2023), this method reproduces winds that track the dominant flow and strength from CESM2 while representing how the flows are disrupted by the islands (Figure 3c). The resulting oceanic circulation forced by the downscaled winds closely resembles the observations. When forced by the CESM2 winds directly, the ocean suffers a significant drop in eddy kinetic energy. More details on the method and results can be found in Liu et al. (2023).

The ocean and atmosphere models of CESM2 are online coupled via the sea surface temperature such that changes in the ocean alter the atmosphere and vice versa; however, for this work, we did not run ROMS online coupled with an atmospheric model. We are specifying the atmospheric conditions as described above, but this poses an issue. The specified atmospheric heat flux is invariant to changes in the ocean, and this imbalance will lead to significant warming or cooling of the ocean over time. This imbalance is not physical, merely a result of a

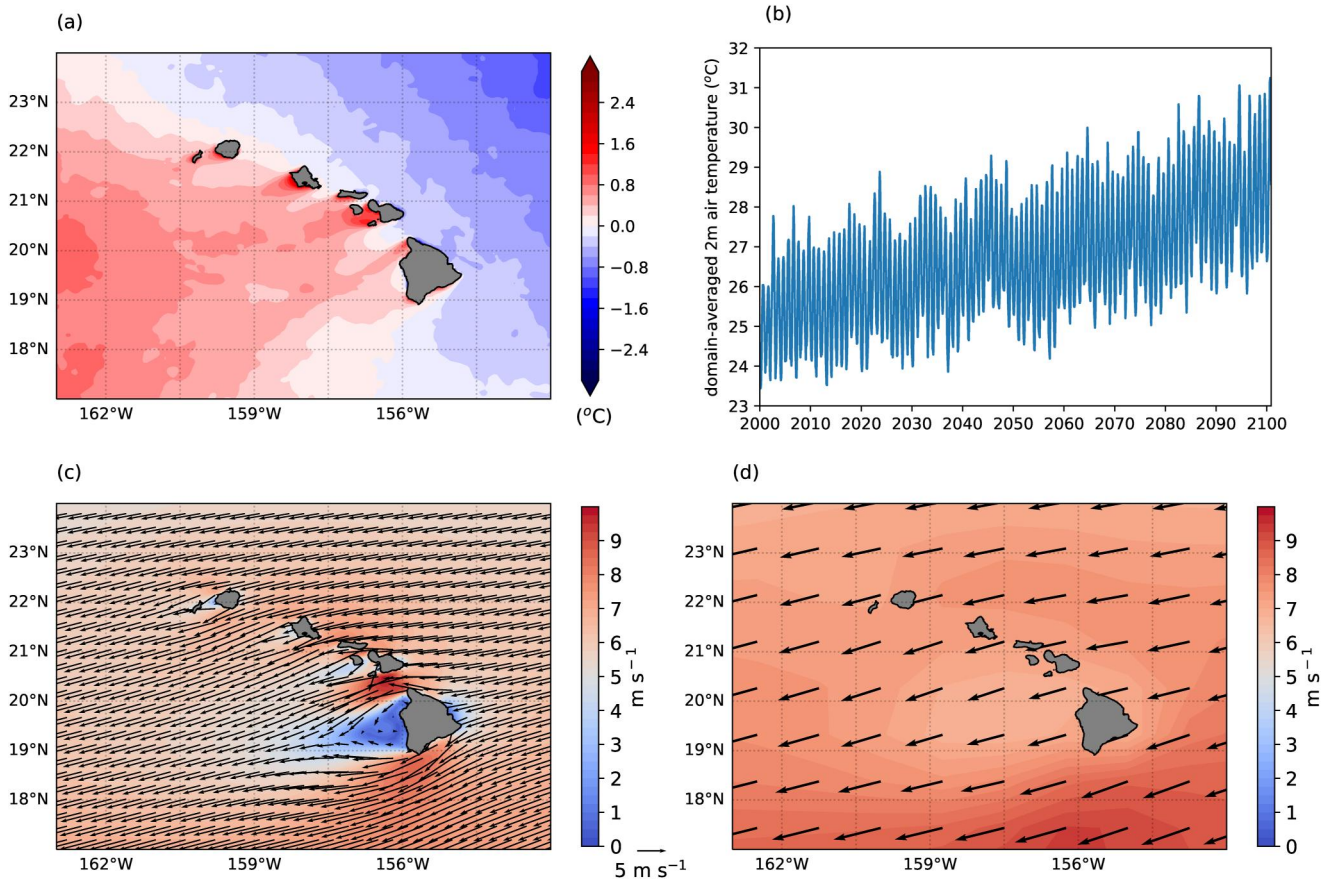

Figure 3. Atmospheric forcing components: (a): snapshot of climatological WRF 2 m air temperature anomaly for September 1 (°C). (b): Domain-averaged CESM2 2 m air temperature (°C) for LE2–1301.009 (SSP3–7.0). (c): Time-averaged (2000–2020) 10 m wind field (m s^{-1}) derived by the neural network. (d): Time-averaged (2000–2020) 10 m wind field (m s^{-1}) of CESM2. See text for details.

fixed atmosphere while the ocean changes underneath it. As such, we employ a heat-flux correction to the atmospheric forcing that is calculated a priori to balance the monthly mean ocean surface temperatures with the heat flux of the atmosphere. These atmospheric heat flux corrections are very weak (average between 0 and −3 W m^{-2}) as compared to the net daily peak heat flux of 800 W m^{-2}. This ensures that there is no artificial warming trend in the ocean from a decoupled atmosphere.

2.3.2. Lateral Boundary Conditions

With the surface atmospheric forcing complete, we now turn to the time-varying oceanic open boundary conditions. As shown in Figure 1, the regional model contains four open ocean boundaries. The physical ocean boundary condition state variables for ROMS (salinity, potential temperature, barotropic and baroclinic current velocities, and sea surface height) are taken from CESM2 monthly mean output for each of the five different CESM2 simulations. The CESM2 fields for each state variable are 3D interpolated using objective analysis (McIntosh, 1990) to map from the CESM2 3D-grid to the ROMS 3D-grid. We then extract the values along the grid boundaries and convert these into ROMS boundary conditions.

Salinity results from all CESM2 simulations show considerable bias in the NPSG as compared to both Station ALOHA and the Global Ocean Data Analysis Project v2.2016b (GLODAP) (Lauvset et al., 2016) with biases ranging from −0.2 to −0.6 psu in the upper 1,000 m (Figure 4a). For all scenarios, we correct the CESM2 bias using spatial salinity data from GLODAP as the reference state. The bias correction is accomplished by: (a) interpolating the GLODAP salinity onto the CESM2 grid locations for our region; (b) calculating the time (2000–2020) mean for each of the CESM2 grid locations; (c) calculating the bias depth-varying between (a) and (b); and, (d) removing this depth-varying bias from all CESM2 output time steps.

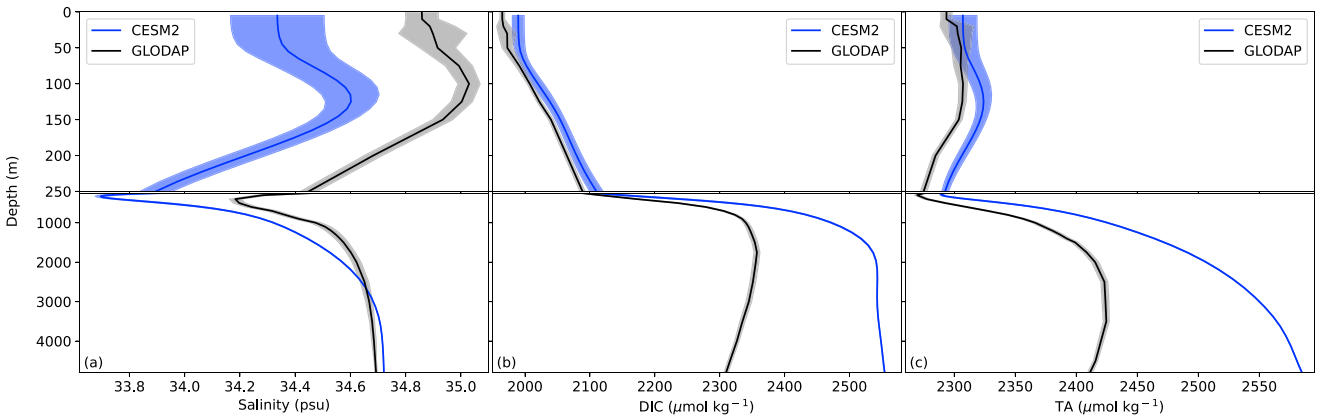

Figure 4. CESM2 biases with respect to Global Ocean Data Analysis Project v2.2016b (GLODAP). (a): Domain-averaged salinity (psu); (b): domain-averaged dissolved inorganic carbon (DIC, μmol kg^{-1}); (c): domain-averaged total alkalinity (TA, μmol kg^{-1}). Shading indicates standard deviations for CESM2 and error estimates provided in the GLODAP data sets.

As discussed earlier, the physical forcing of the CESM2 models well represent the large-scale oceanic and atmospheric flows that are expected for the region, and mapping them onto the regional model (with some bias corrections) is rather straight forward. In contrast, it is not as simple to downscale the biogeochemical variables from CESM2 to ROMS/COBALT.

CESM2 utilizes the Marine Biogeochemistry Library (MARBL) for the ocean ecosystem (Long et al., 2021). This model uses three classes of phytoplankton, one class of zooplankton, as well as four different micro- and macronutrient pools (nitrate, phosphate, silicate and iron), and carbonate chemistry. The ROMS/COBALT model has more constituents (zooplankton, bacterial, and nutrients) than are provided by CESM2/MARBL, and as such, it is necessary to treat each required boundary variable for ROMS/COBALT separately. All variables, unless noted, are first interpolated onto the ROMS grid using the same 3-D objective analysis as is performed with the physical variables.

We begin with the carbonate system variables: DIC and TA. These are taken from CESM2/MARBL and are interpolated to ROMS from the monthly mean output. As compared to GLODAP, both variables exhibit a bias (Figures 4b and 4c), and they are bias corrected using the same method as described for salinity.

Next, we turn to the treatments of micro- and macro-nutrients. In the oligotrophic MHI, phytoplankton growth is severely limited by nutrient availability (typically nitrate, phosphate, and/or iron) (Dave & Lozier, 2010; Letelier et al., 2019). Seemingly minor changes in modeled nitrate can lead to substantial changes in phytoplankton community composition. Therefore, it is imperative that we properly represent the nutrients (with nitrate as the baseline) for the regional simulation.

Examining nitrate, we find that CESM2/MARBL has a limited ability to capture the oligotrophic ecosystem characteristics around the MHI. Near-surface nitrate concentrations simulated by CESM2/MARBL are substantially higher than data provided by GLODAP, in particular in the southern half of the MHI model domain as shown in Figure 5. In particular, the figure shows that the equatorial nitrate maximum extends too far north and into the MHI domain, which is not a locally observed feature and conflicts with GLODAP. Because the CESM2/MARBL simulated MHI are on the gradient between nitrate-rich and nitrate-poor waters, there is very strong interannual variability as the CESM2 simulation meanders waters from high-to-low nitrate in and out of the domain. Unfortunately, these results make it infeasible to use the CESM2/MARBL-derived nutrients (and O_2) directly as abundant nitrate would result in simulating a wrong phytoplankton community composition. What we wish to capture from CESM2/MARBL is the long-term trend in the nutrients.

The COBALT biogeochemistry model is a component of our regional system, so we developed a composite approach with climatological results from a global COBALT retrospective ocean-ecosystem simulation (Stock et al., 2014) from 1988 to 2007 with the CESM2/MARBL long-term trends applied. In summary, we project the COBALT global results (~1° resolution) onto the CESM2 grid (~1° resolution) for our region. We fit a quadratic function to the time-evolving CESM2/MARBL results to generate a trend, scale this trend by the mean ratio of the

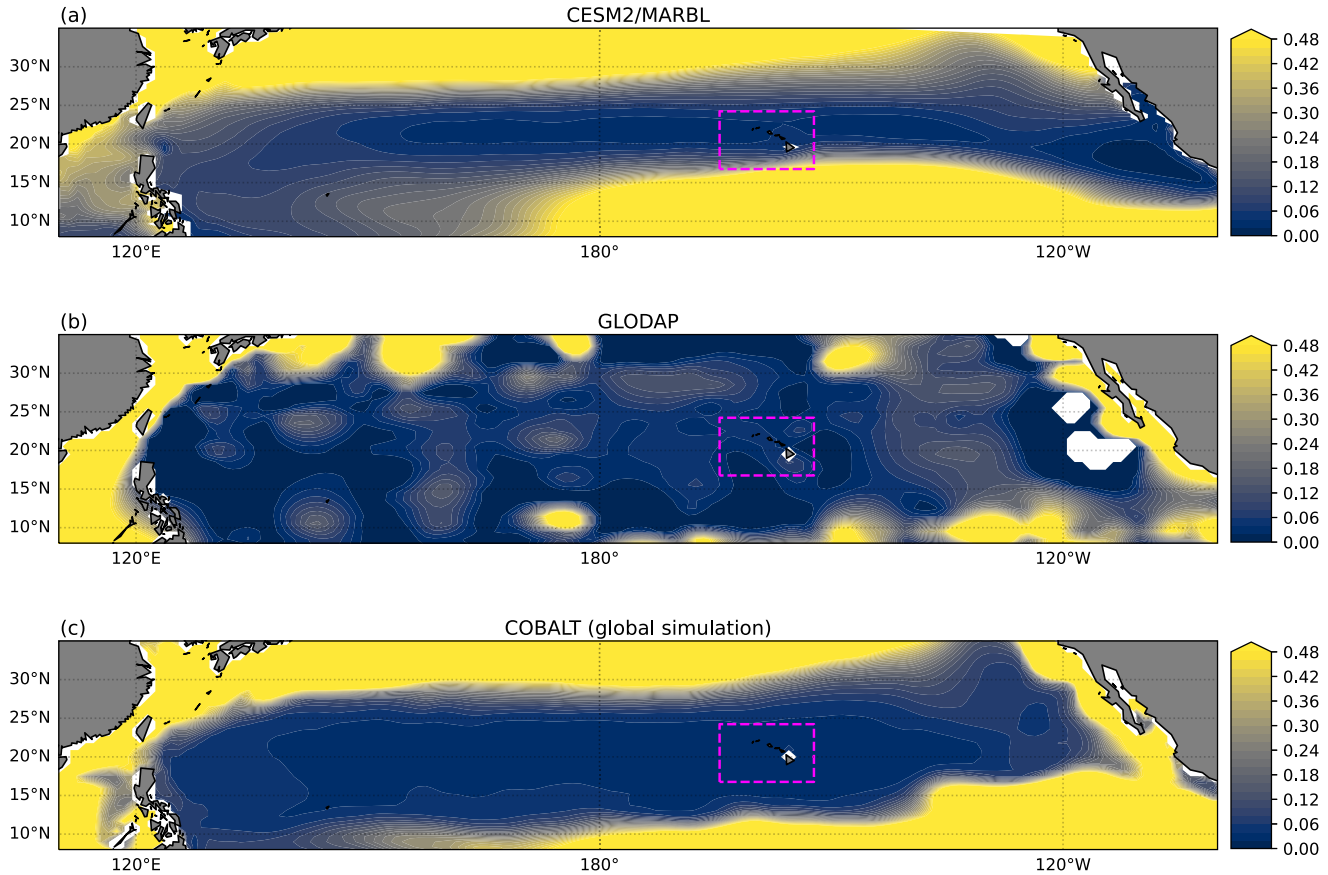

Figure 5. Comparison of time-averaged surface nitrate concentrations (μmol kg^{-1}): (a) CESM2/MARBL, (b) GLODAP, and (c) a global COBALT simulation. White areas in (b) indicate gaps in GLODAP nitrate data. Magenta rectangle indicates regional model domain. See text for details.

two, and add the temporal trend to the COBALT climatology. Finally, we interpolate, the time-evolving data onto ROMS grid. The resulting fields thus have mean levels consistent with the sub-tropical gyre, while deriving the relative trend from CESM2/MARBL.

The first step is to interpolate each COBALT variable with a CESM2/MARBL corollary (nitrate, phosphate, iron, silicate, and oxygen) onto the CESM2 grid using the same objective analysis interpolation as before. We designate the variable of interest as $C(t, x, y, z)$ for COBALT and $M(t, x, y, z)$ for CESM2/MARBL where both are monthly means. The temporal mean of each variable is taken from the periods available. The 20 years mean from COBALT (1988–2007) is given by $\langle C(x,y,z) \rangle$ and the 20 years mean from CESM2/MARBL (2001–2020) is given by $\langle M(x,y,z) \rangle$. While the mean 20 year periods are distinct, Figure 5 reveals a considerable bias between CESM2/MARBL and COBALT that is independent of time. The time-period is chosen for CESM2/MARBL because it overlaps the observational period for the projection period we will be integrating (2000–2100).

The second step is to generate a temporal trend from the CESM2/MARBL results over the 2000 to 2100 period.

The slopes of near-surface variables in the SSP3–7.0 scenario can be estimated by linear trends. However, for deeper layers and values in the low emission scenario SSP1–2.6, a quadratic slope is a better approximation. Consequently, we use ordinary least-squares to fit $M(t, x, y, z)$ with:

$$M(t,x,y,z) \approx \alpha_0 + \alpha_1 t + \alpha_2 t^2, \tag{2}$$

where α are the unknown coefficients and t is the time in months. This produces the temporal quadratic trend for each variable and location in CESM2/MARBL.

Next we apply this trend to COBALT via:

$$\hat{C}(t,x,y,z) = C(t,x,y,z) + \left(\alpha_1 t + \alpha_2 t^2\right) \frac{\langle C(x,y,z)\rangle}{\langle M(x,y,z)\rangle}, \quad (3)$$

where $\hat{C}$ is the COBALT climatology with CESM2/MARBL trend applied. The trend is scaled by the ratio of the temporal means so that the trend is appropriate to the mean value of COBALT; otherwise, the trend will lead to unreasonable solutions in time (again, due to the misrepresentation of the NPSG biogeochemistry by CESM2/MARBL).

Once all monthly $\hat{C}(t,x,y,z)$ values are generated, they are interpolated by objective analysis onto the ROMS grid.

The final set of ecosystem variables are not available from CESM2/MARBL. These variables mainly comprise phytoplankton and zooplankton concentrations as well as the different organic matter pools. They are taken from the global COBALT simulation. These are applied in the same fashion as described in Friedrich et al. (2021). They are interpolated via objective analysis onto the ROMS grid and used directly. Because these are monthly climatologies, this means that these ecosystem variables are prescribed the same throughout the century (e.g., every January is forced the same). They follow a seasonal cycle, but do not follow any interannual variability or future trends. While this may seem counter-intuitive, the time-scales over which the surface plankton handled in this way respond to changes in nutrients and physical factors that have imposed trends is generally short. Thus, any reasonable boundary value for these properties will settle onto interior values consistent with imposed multi-decadal nutrient and physical trends over time scales ranging from days to months. This allows us to examine how these constituents evolve dynamically within the regional domain and due to changes that may occur locally.

2.4. Initial Conditions

Initial conditions follow the same composite approach as outlined for boundary conditions. Monthly mean, bias-corrected CESM2 fields corresponding to January 2000 were used and interpolated to the ROMS/COBALT grid.

All ROMS/COBALT simulations begin 1 January 2000, and are integrated for 101 model years until the end of year 2100. Output consists of daily means of all relevant physical and biogeochemical variables as well as hourly data for the Station ALOHA location.

3. Results and Discussion

Using the methodology above, we produce five sets of initial conditions, lateral boundary conditions, and atmospheric forcing for the five separate CESM2 projections. These are used to produce five separate ROMS/COBALT projections for the MHI. We now evaluate those solutions to examine whether they provide valid solutions. The dynamical downscaling has to meet two criteria in order to be used as credible projections for our region. First, the regional model results for the observed period (2000–2022) have to be in reasonable agreement with observations. Second, domain-averages of regional downscaling have to follow the large-scale trends and variability as is present in CESM2. It is noted that neither ROMS/COBALT or CESM2 use any form of data assimilation and are freely running.

In this section, we present results with respect to each of the criteria followed by an overview of climate change projections for the MHI as produced by ROMS/COBALT to illustrate the benefit of the downscaling.

3.1. Model to Observation Comparison

Station ALOHA is located within the MHI domain (Figure 1) and for the first 21 years (2000–2020) of the simulations, quality-controlled HOT observations are available to evaluate the results of both ROMS/COBALT and CESM2. The temporal evolution of SST at the Station ALOHA location is well captured by both models (Figure 6a). The average SST for the 2000–2020 period amounts to 25.1°C for HOT compared to 24.7 and 24.9°C for ROMS/COBALT and CESM2 respectively. A decomposition of the SST evolution into a linear trend and a seasonal cycle reveals that observations and model results share an identical warming trend of ∼0.31°C/decade. Furthermore, the amplitude and phase of the seasonal cycle are similar (Figure 6c). In the vertical, both models exhibit good agreement with observations and capture the time-averaged vertical profile of temperature very well (Figure 7a).

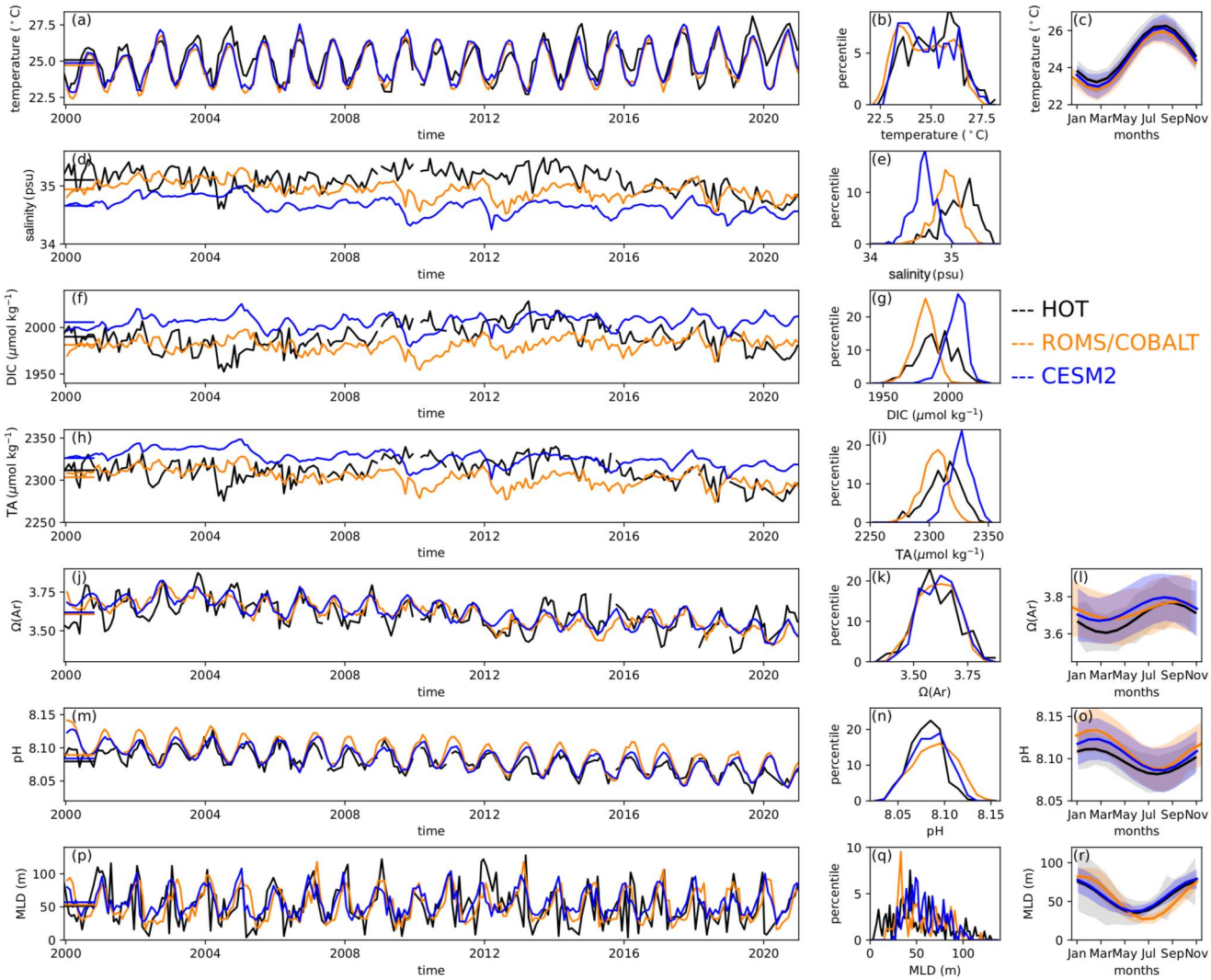

Figure 6. Comparison of surface data for the Station ALOHA location for observations (black), ROMS/COBALT (orange) and CESM2 (LE2–1301.009, blue). Left column: Time series comparison. Horizontal bars on the left indicate temporal mean for the time period shown. Middle column: histograms of surface data, and right column: mean annual cycle (where applicable) and standard deviation (shaded) of mean annual cycle. Row 1 (a–c): temperature (°C), row 2 (e, d): salinity (psu), row 3 (f, g): dissolved inorganic carbon (DIC, μmol kg^{-1}), row 4 (h, i): total alkalinity (TA, μmol kg^{-1}), row 4 (j–l): aragonite saturation (Ω_{A_r}), row 5 (m–o): pH, and row 6 (p–r) mixed layer depth (MLD, m).

Comparing simulated salinity to HOT data, again reveals the bias in CESM2. Our regional model yields a much better representation of salinity observations as a consequence of using bias-corrected boundary and initial conditions. The time-averaged Sea Surface Salinity difference with respect to observations at Station ALOHA amounts to 0.1 psu and it remains unclear how much of this mismatch can simply be attributed to differences in interannual variability between ROMS/COBALT and HOT because the magnitude of these longterm changes are substantial in the NPSG (Hu et al., 2020; Lukas, 2001). The vertical profile of salinity is well captured by ROMS/COBALT (Figure 7b). Combining salinity and temperature data, it can be seen that our bias-corrected regional model exhibits a good representation of the watermass structure at Station ALOHA (Figure 7c); whereas, CESM2 results are offset with respect to salinity in the temperature range above 5°C (approximately above 1,500 m).

The use of bias-corrected boundary conditions also helps to improve the representation of DIC and TA. Surface values of DIC and TA simulated by CESM2 are slightly too high (Figures 6f–6i) and deep-ocean values are higher than observations (Figures 7d and 7e). ROMS/COBALT exhibits a much better agreement with HOT data. The subsurface TA minimum is well captured by our regional simulation. Temporal variability of DIC and TA simulated by ROMS/COBALT at the surface is lower compared to the observed one (Figures 6g and 6i).

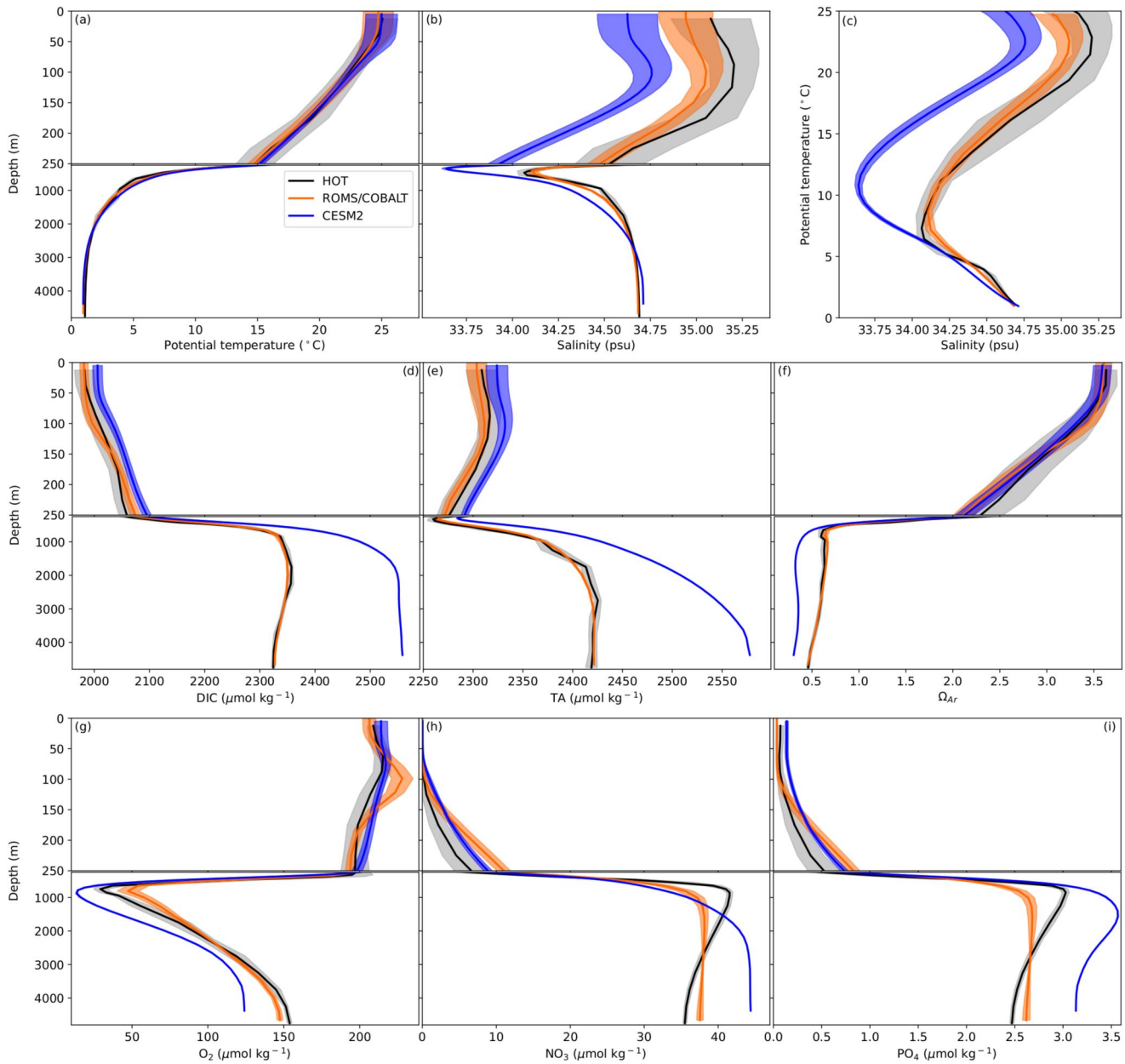

Figure 7. Comparison of time-averaged (2000–2020) profile data for the Station ALOHA location for observations (black), ROMS/COBALT (orange), and CESM2 (LE2–1301.009, blue). Variables as indicated in the panels. Shading corresponds to the temporal standard deviation at the respective depth.

Surface values of the aragonite saturation state (Ω_{Ar}) and pH modeled by CESM2 and ROMS/COBALT are in good agreement with observations (Figures 6j–6o). The time-averaged pH simulated by ROMS/COBALT for the Station ALOHA location is about 0.01 too high, which is a direct consequence of the DIC of the slight bias of -8 μmol kg^{-1}. The temporal trends for the year 2000–2020 period amount to -0.08/decade (HOT), -0.10/decade (ROMS/COBALT), and -0.11/decade (CESM2) for Ω_{Ar} and 0.017/decade (HOT), 0.020/decade (ROMS/COBALT), and 0.020/decade (CESM2) for pH respectively. The observed vertical profile of Ω_{Ar} is well captured by ROMS/COBALT (Figure 7f). Deep-ocean Ω_{Ar} values simulated by CESM2 are too low due to the significant DIC bias at these depths.

Mixed-layer depth is calculated based on the location of the 0.2°C temperature difference (de Boyer Montégut et al., 2004). This is somewhat temporally noisy in particular for observational data (Figures 6p and 6r), but reveals that ROMS/COBALT captures the overall amplitude and seasonality of observed mixed layer depth.

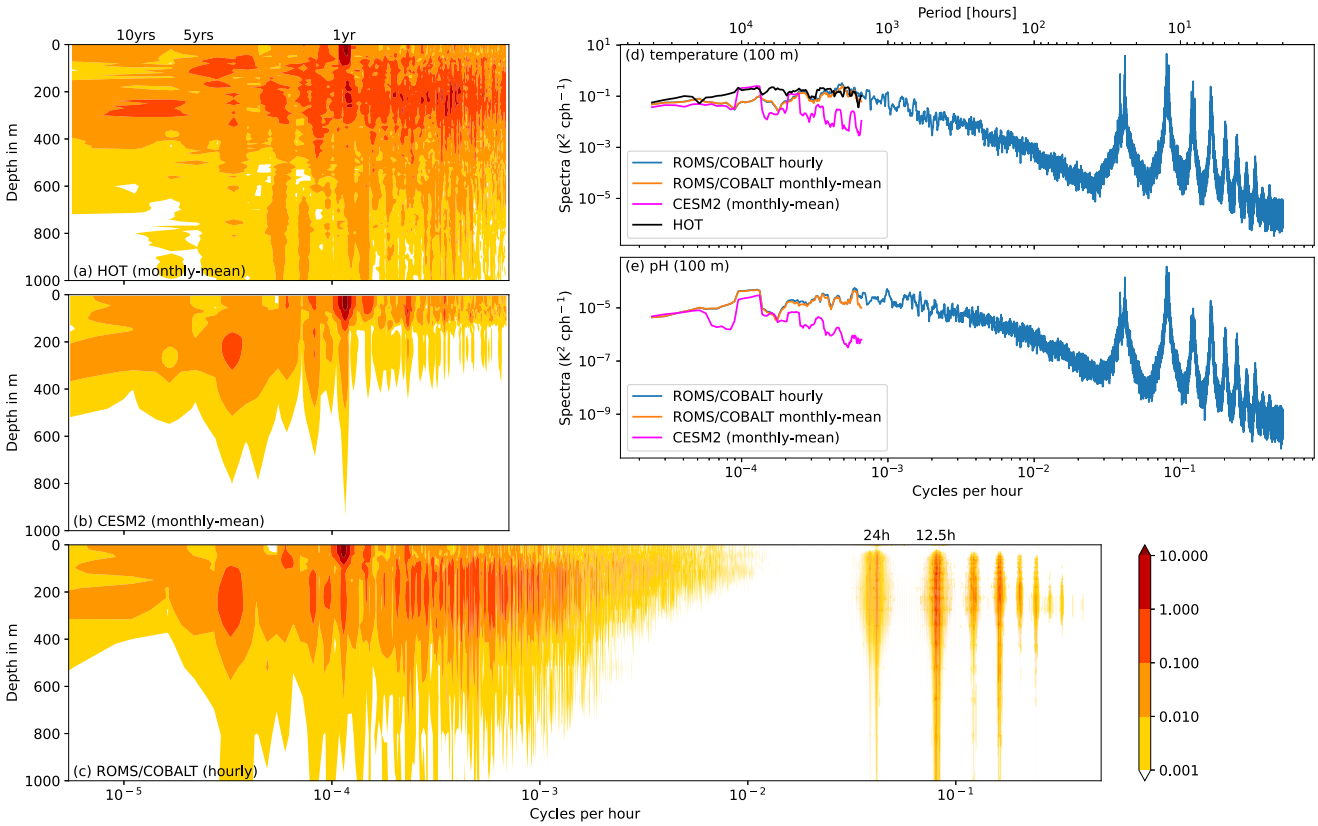

Figure 8. Power spectrum for temperature (°C^2, a–d) and pH (e) at Station ALOHA location. Power spectrum for temperature as a function of depth for HOT (a), monthly mean CESM2 data (b), and hourly ROMS/COBALT data (c). (d): Power spectrum at 100 m depth for hourly ROMS/COBALT data (blue), monthly mean ROMS/COBALT data (orange), monthly mean CESM2 data (magenta), and HOT observations (black). (e): Same as (d) for pH. Note that sufficient pH data was not available for HOT for 100 m water depth. All spectra are based on detrended data for the years 2000–2020.

The oxygen profile at Station ALOHA is well captured by our simulation (Figure 7g) including the location of the oxygen minimum zone. However, the simulated minimum has a value of ∼50 μmol kg^{-1} as compared to the measured minimum of ∼35 μmol kg^{-1}. We believe that this mismatch is mainly a result of the vertical resolution of the model that is in the order of ∼150 m at a depth of 900 m and cannot capture the large vertical gradients seen for oxygen, leading to a smoothing of the profile. A similar problem arises for nitrate and phosphate (Figures 7h and 7i). Here, the maxima that are observed at around 900 m water depth are not as pronounced.

Overall it can be noted that the treatment of salinity, DIC, TA, oxygen and nutrients described in Section 2 leads to a better agreement of our ROMS/COBALT run with observations as compared to the CESM2 output.

For each of our ROMS/COBALT downscaled projections, we save full water column output at the location of Station ALOHA every hour. We calculate the spectral densities as a function of depth for the years 2000–2020 for simulated detrended temperature using hourly ROMS/COBALT data and monthly mean CESM2 output for the Station ALOHA location as well as HOT observations with approximately monthly resolution (Figures 8a–8c). The spectral energy at the surface, is dominated by the annual cycle for all three data sets. Temperature observations also exhibit a considerable amount of spectral energy at sub-annual timescales and water depths of 50–500 m. This is well captured by ROMS/COBALT. For CESM2, however, a strong decrease in sub-annual spectral energy can be seen at around 150 m depth. The spectra of the hourly ROMS/COBALT output clearly show that a large amount of spectral energy is also present at tidal frequencies (Figure 8c) indicating that tidally driven processes contribute substantially to temperature variance in the upper ∼500 m. These processes are not captured by CESM2 since no tidal forcing is present in this model.

At 100 m water depth spectral energy at tidal frequencies dominates the spectra of temperature and pH for ROMS/COBALT (Figures 8d and 8e) (Please note that a spectral density for pH at 100 m could not be calculated due to a

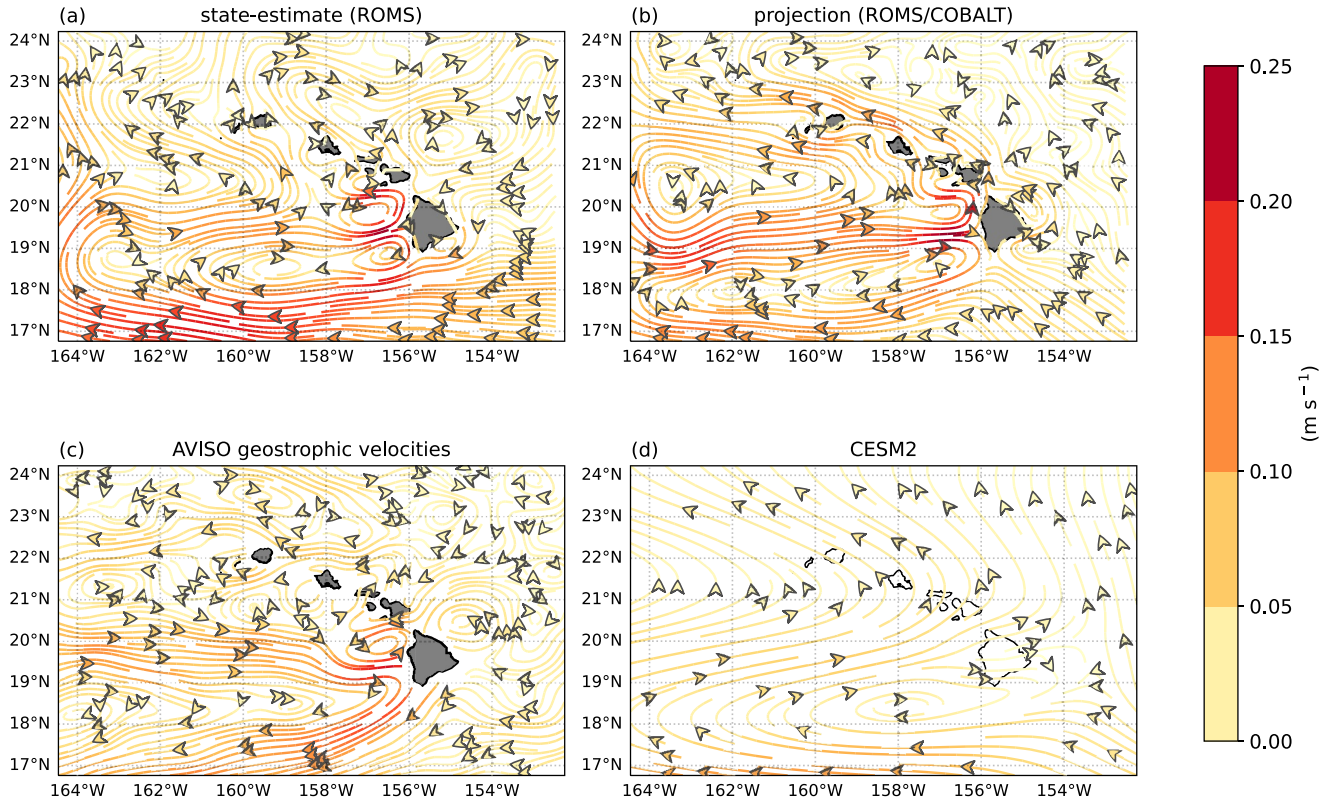

Figure 9. Comparison of time-averaged (years 2010–2020) upper ocean currents (0–100 m, m s^{-1}) for (a) ROMS state estimate (Partridge et al., 2019), (b) ROMS/COBALT downscaled within CESM2, (c) AVISO geostrophic currents, and (d) CESM2 (LE2–1301.009).

lack of data.). When comparing the monthly mean CESM2 and ROMS/COBALT data it becomes apparent that CESM2 accounts only for 38.6% (19.3%) of the spectral power of temperature (pH) seen in ROMS/COBALT. Compared to the observation-based spectrum, both models tend to underestimate temperature variance in the frequency band covered by the measurements.

3.2. CESM2 to ROMS/COBALT Comparison

As discussed, the tall mountains of the Hawaiian archipelago exert a considerable impact on the wind patterns and structure of upper ocean (integrated 100 m) currents as well as location and magnitude of mesoscale variability occurring in our domain. To assess the performance of ROMS/COBALT (and CESM2) in representing the upper current structure, we compare it against AVISO geostrophic currents (AVISO, 2023) and a state-estimate reanalysis using more than 65 million physical observations (Friedrich et al., 2021; Partridge et al., 2019) that was conducted for years 2010–2020. As can be seen from the AVISO geostrophic velocities and described in Section 1, the near-surface current structure in our domain is characterized by the bifurcation of NEC in the east as well as the shear zone between the NEC and the HLCC to the west of the island of Hawai'i (Figure 9c). These features are well represented in both the state-estimate reanalysis as well as our downscaled projection (Figures 9a and 9b).

Differences between the current structures exist near the eastern boundary where the flow of the NEC appears to be stronger in the reanalysis. Also, the recirculation of the NHRC in the north-eastern corner of the domain is less developed in the downscaled projection. It should be noted however, that those are minor differences that are due to the use of different boundary conditions and wind forcing. A bifurcation of the NEC is not visible in CESM2 (Figure 9d) and an NHRC cannot be identified. The HLCC is substantially weaker and no HLC is present and it can be concluded that the careful treatment of the windfield as well as the fully resolved mesoscale of ROMS/COBALT results in a more realistic flow structure as compared to CESM2.

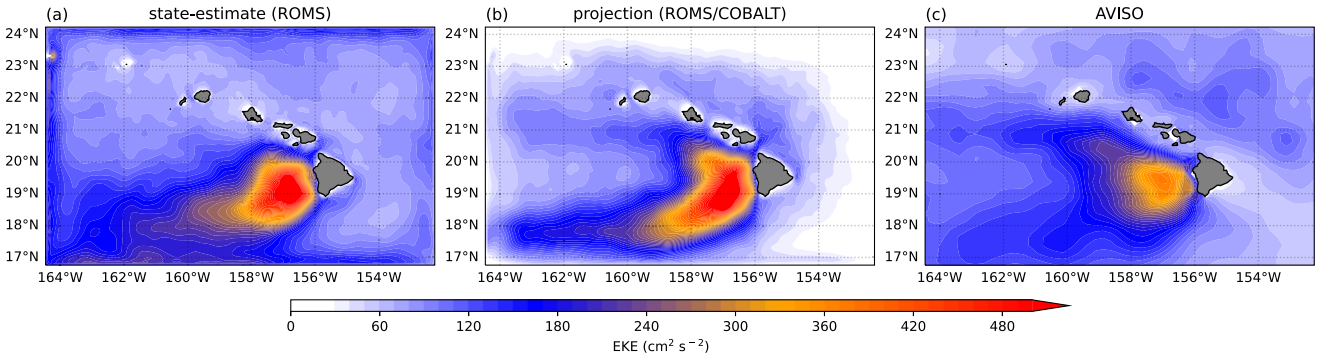

Figure 10. Comparison of mean eddy kinetic energy (EKE, $cm^2\ s^{-2}$) for (a) ROMS state estimate (Partridge et al., 2019), ROMS/COBALT downscaled within CESM2 (b) and (c) AVISO geostrophic velocities (AVISO, 2023). EKE was calculated over the mixed layer for ROMS based on daily averages. All three EKE data sets were averaged for the time period 2010–2020.

In the direct lee of the island of Hawai'i, the eddy variability is due to the 60-day period of the wind stress curl (Calil et al., 2008; Yoshida et al., 2010), and the resulting eddies and fronts have a strong impact on mixing of ocean constituents and particularly on biogeochemical tracers. Using eddy kinetic energy (EKE) as a metric it can be seen that magnitude and spatial structure of mesoscale and submesoscale variability is well captured by our simulation (Figure 10). The EKE maximum is found to the west and south-west of the island of Hawai'i with values ranging between ~200–500 $cm^2\ s^{-2}$ (when calculated over the mixed layer). This is in good agreement with values calculated from AVISO observations of geostrophic currents (Figure 10c) and previous studies (see Calil et al. (2008), their Figures 2 and 6).

The strong wind stress curl in the lee of the island of Hawai'i also has a significant impact on temperature, productivity and marine chemistry of the region (shown for SST: Figures 11a and 11b). The enhanced EKE in cyclonic regions cools the water and doming of isopycnals leads to enhanced productivity, whereas anticyclonic regions have increased temperatures and tend to suppress algae blooms. Furthermore, in the direct lee of the island that is sheltered from the winds, the temperature variability is greater without the heat loss due to the winds. This means that through the HLCC region, stronger variability in ocean physics and biogeochemistry is observed. By missing these dynamics the CESM2 output exhibits only weak and spatially uniform variabilities for these variables on sub-annual timescales (Figures 11c and 11d). The ROMS/COBALT downscaling represents these processes resulting in much higher temperature variability in the HLCC region and compares well to the ROMS/COBALT state estimate as well as satellite measured variability.

The enhanced productivity and increased spatially non-uniform variability in numerous constituents are defining features of our domain. By capturing these critically important processes, the downscaled model adds significant value and robustness to the large-scale variability and trends represented by CESM2.

3.3. Domain-Averaged Trends and Variability

We have shown that the regional model produced with this methodology described is able to reproduce most significant dynamics from tides to mesoscale around the MHI and that both the physical and biogeochemical results capture the processes observed at Station ALOHA. In addition, we must ensure that the regional model does not deviate from the large-scale processes (planetary flows and interannual processes) and trends that are resolved and prescribed by the CESM2 model forcing. For this comparison, we turn to domain-wide averages in order to eliminate the spatial variability that the regional model is contributing.

Atmospheric CO_2 concentrations vary widely between the three SSP scenarios reaching a difference of 426 ppmv by the end of the century (Figure 12a). Values for the SSP1–2.6 scenario reach a maximum of 474 ppmv in the year 2063 and then fall to 445 ppmv by the year 2100. The maxima for the other two scenarios are 603 ppmv (SSP2–4.5) and 871 ppmv (SSP3–7.0) respectively. The corresponding SST increase ranges between 1.64 and 3.25°C (see Table 2). Near-surface (0–50 m) temperature simulated by CESM2 for our domain is not only characterized by a warming trend but is also subject to considerable interannual and decadal variability (Figure 12b). In fact, due to this natural variability it is virtually impossible to distinguish between the different warming scenarios until the year 2080. Our regional simulations capture all these features very well and follow

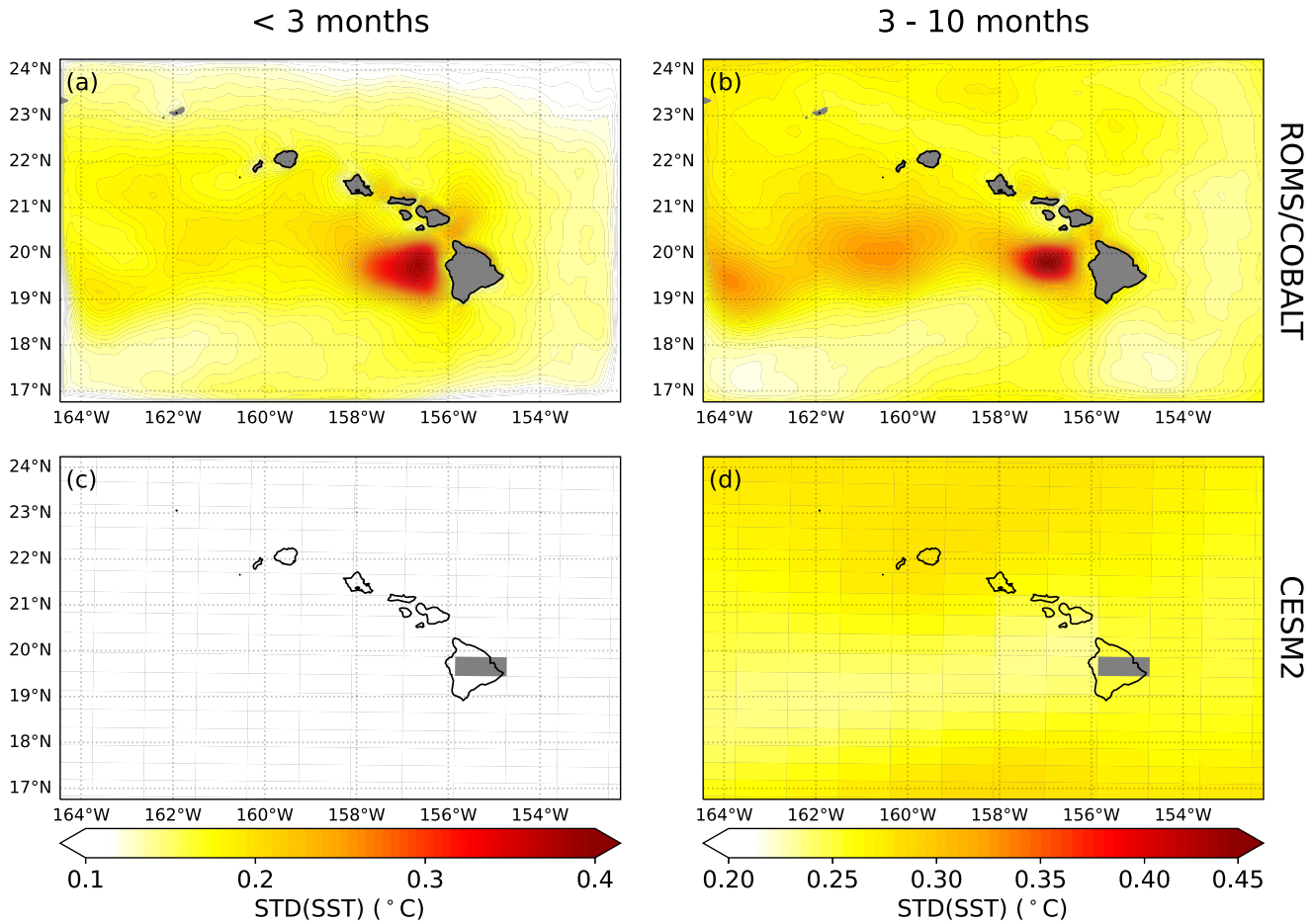

Figure 11. Comparison of sub-annual SST variability for ROMS/COBALT (upper row) and CESM2 (lower row). (a) Standard deviation of detrended 3 months high-pass filtered ROMS/COBALT SST (°C). (b) Standard deviation of detrended 3–10 months band-pass filtered ROMS/COBALT SST (°C). (c and d): Same as (a) and (b) for CESM2 (member LE2–1301.009). A least-square quadratic fit was applied to simulated SST prior to filtering to account for the anthropogenic trend by removing the quadratic slope.

the large-scale temperature evolution of CESM2 very closely. The correlations for the (detrended) near-surface domain-averaged temperature evolutions amount to 0.99 for all simulations (Table 3) However, all simulations are subject to a small bias in domain-averaged near-surface temperature of ∼0.4°C. This bias can be attributed to energetic and radiative imbalances between CESM2 and ROMS/COBALT that result from the downscaling method.

Interannual-to-interdecadal near-surface salinity variations simulated by CESM2 (bias-corrected) reach amplitudes of up to 0.8 psu in the domain-average (Figure 12c). A long-term near-surface salinity trend cannot be identified for any of the scenarios. ROMS/COBALT captures the interannual-to-interdecadal near-surface salinity swings very well with correlations ranging between 0.97 and 0.99 an a bias range of 0.06–0.08 psu (Table 3).

Domain-averaged near-surface DIC and pH are largely dominated by the anthropogenic trend and exhibit relatively small interannual variability (Figures 12d and 12e). Our model results follow CESM2 very closely (correlations 0.90–0.99, Table 3) and the biases of ∼3 μmol kg^{-1} (DIC) and ∼0.005 (pH) are negligible.

As a consequence of the good representation of CESM2's interannual variability by ROMS/COBALT, our downscaling efforts can also capture the spread between the three SSP3–7.0 simulations which can be regarded as a measure of uncertainty for the projections linked to internal climate variability. This spread can reach values of 1.4°C for near-surface temperature and hence about half of the projected overall warming (Figure 12b). The correlations between the spreads simulated for temperature, salinity, and DIC amount to 0.96–0.98. Only for pH

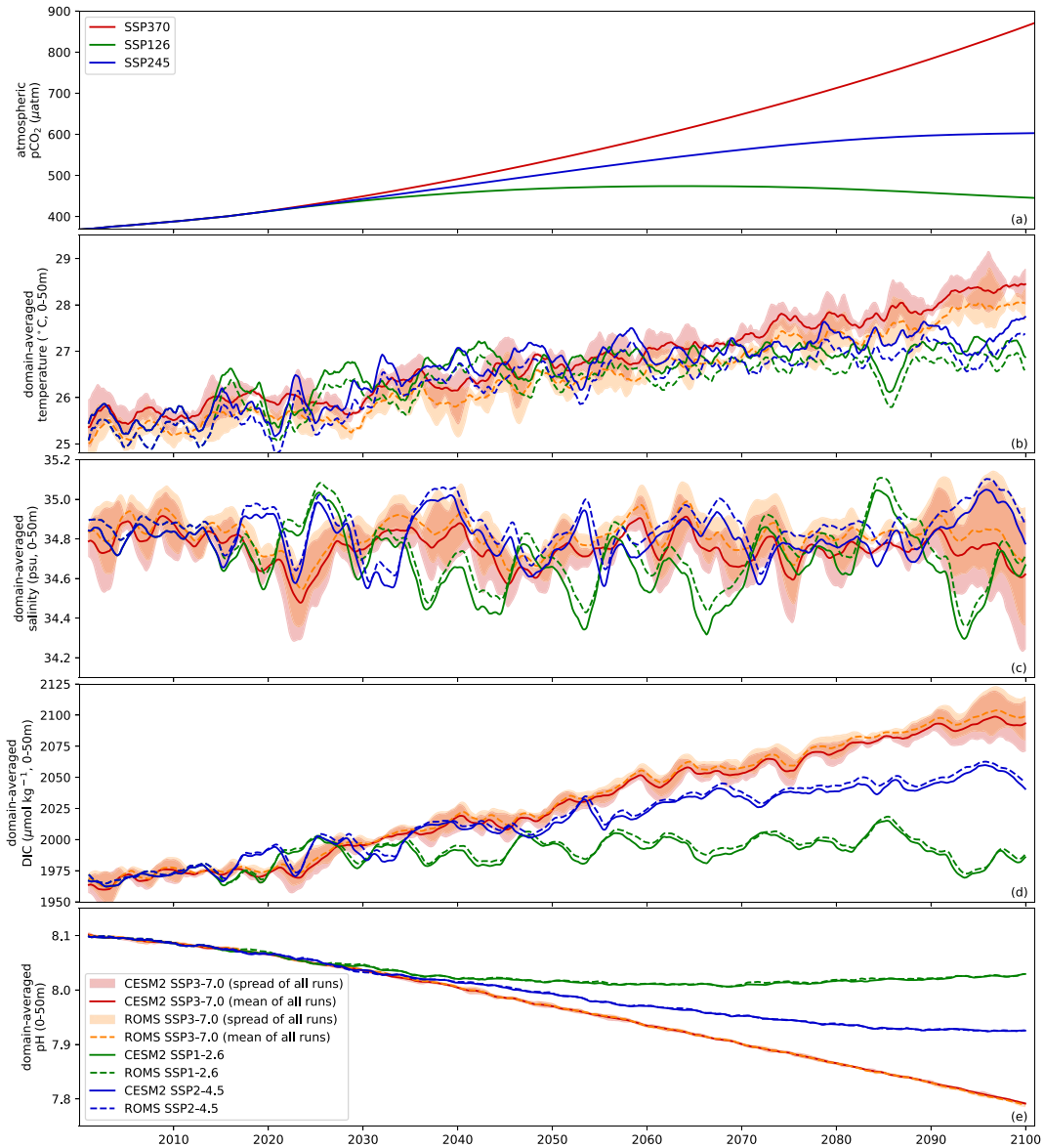

Figure 12. Comparison of near-surface (0–50 m) domain averages for CESM2 (solid lines) and ROMS/COBALT (dashed lines). Variables and scenarios as indicated in the panels. Shading corresponds to the spread of the three SSP3–7.0 simulations. A smoothing window of 24 months was applied for clarity.

the correlations is lower (0.68). However, interannual variability and ensemble spread are extremely small for domain-averaged pH which is in agreement with projected global-scale surface pH evolution (Frölicher et al., 2016).

3.4. Overview of Downscaled Climate-Change Projections

Ocean warming and acidification will likely have widespread effects on stratification, nutrient cycling, primary productivity, marine chemistry and more for the MHI. Presenting a comprehensive assessment of these effects for the different scenarios is beyond the scope of this methodological study, and will be subject of our future publications. In this section, we provide a brief and preliminary overview of some results focusing on coastal temperature and pH.

The projected domain-averaged surface ocean warming is in the order of 3°C by the end of the 21st century for the SSP3–7.0 scenario (Table 3, Figure 12). It can be seen that spatial differences in the warming are relatively weak

Table 3
Correlation, RMSE, and Bias for Detrended Near-Surface (0–50 m) Domain-Averaged Variability for CESM2 and ROMS/COBALT (Detrended Time Series Shown in Figure 12)

Simulation	Variable	Correlation	RMSE	Bias
SSP3–7.0	Temperature	0.99	0.40°C	−0.40°C
LE2–1301.009	Salinity	0.97	0.07 psu	0.06 psu
	DIC	0.98	3.31 μmol kg^{-1}	2.79 μmol kg^{-1}
	pH	0.90	0.006	−0.005
SSP3–7.0	Temperature	0.99	0.40°C	−0.40°C
LE2–1231.003	Salinity	0.98	0.09 psu	0.08 psu
	DIC	0.98	4.27 μmol kg^{-1}	3.84 μmol kg^{-1}
	pH	0.95	0.006	−0.005
SSP3–7.0	Temperature	0.99	0.38°C	−0.38°C
LE2–1231.010	Salinity	0.97	0.08 psu	0.08 psu
	DIC	0.98	2.77 μmol kg^{-1}	2.26 μmol kg^{-1}
	pH	0.95	0.004	−0.003
CMIP6-historical.011/CMIP6-SSP1–2.6.102	Temperature	0.99	0.38°C	−0.38°C
	Salinity	0.99	0.08 psu	0.07 psu
	DIC	0.98	2.89 μmol kg^{-1}	2.26 μmol kg^{-1}
	pH	0.94	0.004	−0.004
CMIP6-historical.011/CMIP6-SSP1–4.5.102	Temperature	0.99	0.40°C	−0.39°C
	Salinity	0.98	0.08 psu	0.07 psu
	DIC	0.97	3.15 μmol kg^{-1}	2.70 μmol kg^{-1}
	pH	0.97	0.005	−0.005

Note. A smoothing window of 24 months was applied. The bias was calculated as the difference between ROMS/COBALT and CESM2.

with a total range of ∼2.85–3.30°C for the LE2–1301.009 member (Figures 13a and 13d). For CESM2, the spatial structure of the anthropogenic warming is characterized by a simple northwest-to-southeast gradient. Our downscaled projection show that the presence of the islands lead to a much more complex warming pattern with a maximum that extends out westwards from the Island of Hawai'i. The differences between CESM2 and ROMS/COBALT become even more noticeable when we take into account the (spatially varying) standard deviation of SST (Figures 13b and 13e) to put the warming signal into the context of natural variability. The natural variability of SST in CESM2 is mostly dominated by the amplitude of the seasonal cycle that is larger in the northern part of the domain. As a consequence, the spatial structure of CESM2's warming-to-variability ratio exhibits a similar gradient as for the warming itself (Figure 13c) with values ranging between 1.5 and 2.7.

The overall spatial structure of natural variability of SST in ROMS/COBALT is similar to that of CESM2. However, activity of mesoscale eddies generate a local maximum to the west of the island of Hawai'i (see also Figures 11a and 11b). As a result—and different from CESM2—, areas with the largest warming-to-variability ratio (Figure 13f) do not necessarily overlap with the strongest warming. Furthermore, the warming-to-variability ratio is larger in ROMS/COBALT in particular in the southern half of our domain.

The spatial resolution of the downscaled projections allows us to specifically investigate changes in coastal ocean points. The coastlines of the MHI are home to coral reef ecosystems that are critical for biodiversity, tourism, coastal protection and more. Climatic changes that impact corals along the coastline are of particular importance.

NOAA defines the threshold for coral bleaching based on coastal SSTs exceeding the local highest monthly mean temperature by 1°C (Glynn & D'croz, 1990). Averaging over 461 coastal grid points of the regional model for a reference period of 2011–2020, the highest monthly mean near-surface (0–50 m) temperature amounts to 26.6°C with a range of 25.8–27.4°C. Here, we choose the highest value of 27.4°C as a baseline for a conservative estimate which sets the bleaching threshold to 28.4°C. The likelihood of temperatures exceeding this threshold during the

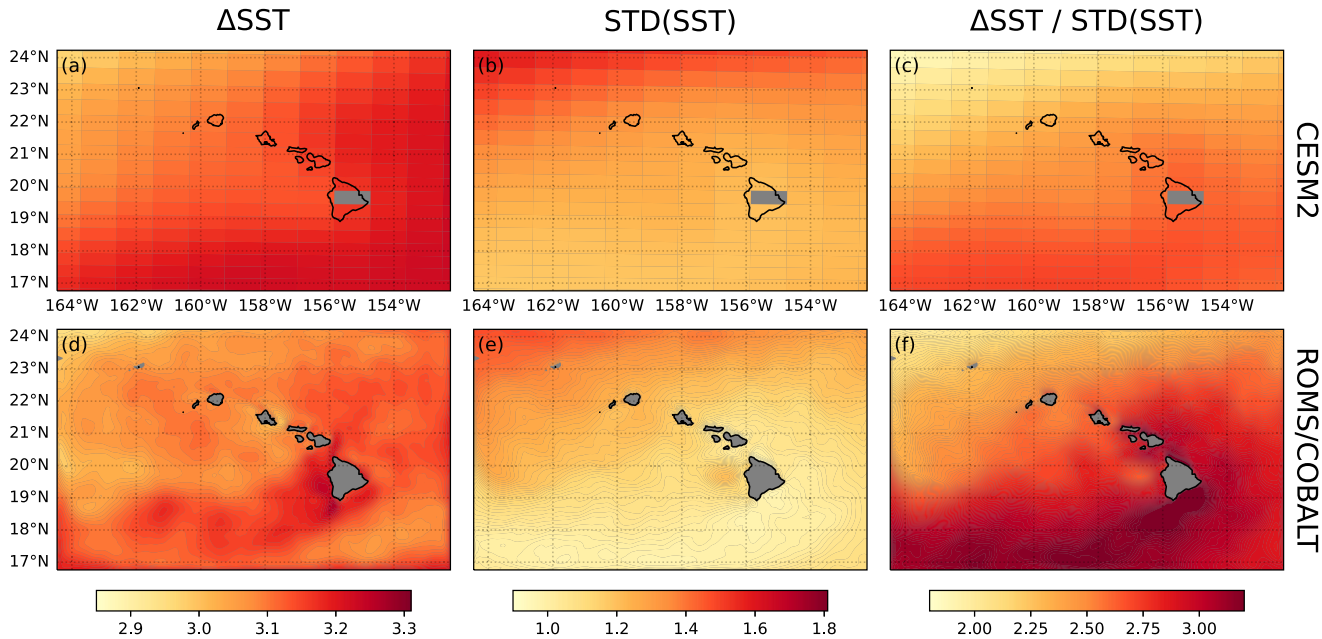

Figure 13. Anthropogenic warming, natural variability and warming-to-variability ratio for SSP3–7.0 simulation (member LE2–1301.009). (a) 21st century SST increase simulated by CESM2, (b) standard deviation of SST in CESM2, (c) ration of 21st century SST increase and standard deviation of SST for CESM2. (d–f) Same as (a–c) for ROMS/COBALT. Standard deviation was calculated based on detrended daily SST averages for the years 2011–2020.

2011–2020 time period within coastal grid cells is ~0.06% (Figures 14a and 14c). By the end of the 21st century, this changes significantly. Coastal near-surface temperatures average 27.9 ± 1.19°C in the mean of the three downscaled SSP3–7.0 scenario (Figure 14a, Table 4). The likelihood of temperatures exceeding a threshold of 28.4°C increases more than five-hundred-fold to ~34.6%. It should be noted, however, that this calculation is based on a fixed temperature threshold and does not take into account potential adaptation to the warming.

The maximum changes in the SSP1–2.6 and SSP2–4.5 scenario are relatively similar to each other when near-surface coastal temperatures are considered (Figures 14a and 14c; Table 4) with a mean warming increases of 1.05 and 1.47°C respectively.

The differences between scenarios become substantially more pronounced when it comes to projections of marine carbon chemistry (Figures 14b and 14d). In the lowest emission scenario, coastal near-surface pH decreases by 0.07, corresponding to a 16.6% increase in H^+ ion concentration and ~4 times the standard deviation of the pH-distribution simulated for the reference period (Figure 14b; Table 4). These changes double for the SSP2–4.5 scenario. By contrast, the SSP3–7.0 scenario atmospheric CO_2 concentrations reach values of >860 ppmv at the end of the century, which results in a pH decrease of 0.27 in the coastal ocean. The associated shift in carbonate chemistry corresponds to more than 16-times the standard deviation of the pH-distribution of the reference period and a 87.1% increase in H^+ ion concentration. When using pH as a metric for the state of marine carbon chemistry, our simulations suggest that end-of-century conditions will share no overlap with present-day conditions under the SSP2–4.5 or SSP3–7.0 scenarios (Figures 14b and 14d).

The drastic decrease in pH is associated with significant decreases in aragonite saturation state and the substrate-to-inhibitor ratio (Bach, 2015; Cyronak et al., 2016) (Table 4) that have both been used as proxies for coral reef calcification rates. Even though the exact role of ocean acidification in future reef calcification rates remains elusive (Bahr et al., 2017, 2018; Bove et al., 2020), numerous studies found empirical relationships between aragonite saturation state and calcification (Albright et al., 2016, 2018; Chan & Connolly, 2013; Langdon & Atkinson, 2005) that range between 15% and 43% change in calcification per unit Ω_{Ar}. In view of these findings, it has to be expected that the projected changes in coastal Ω_{Ar} of −0.71 (SSP2–4.5) and −1.25 (SSP3–7.0) as well as a ~40% drop in the substrate-to-inhibitor ratio (Table 4) would have a substantial negative effect on the wellbeing of coral reefs in Hawaiian waters that will most likely be exacerbated by the significant ocean warming.

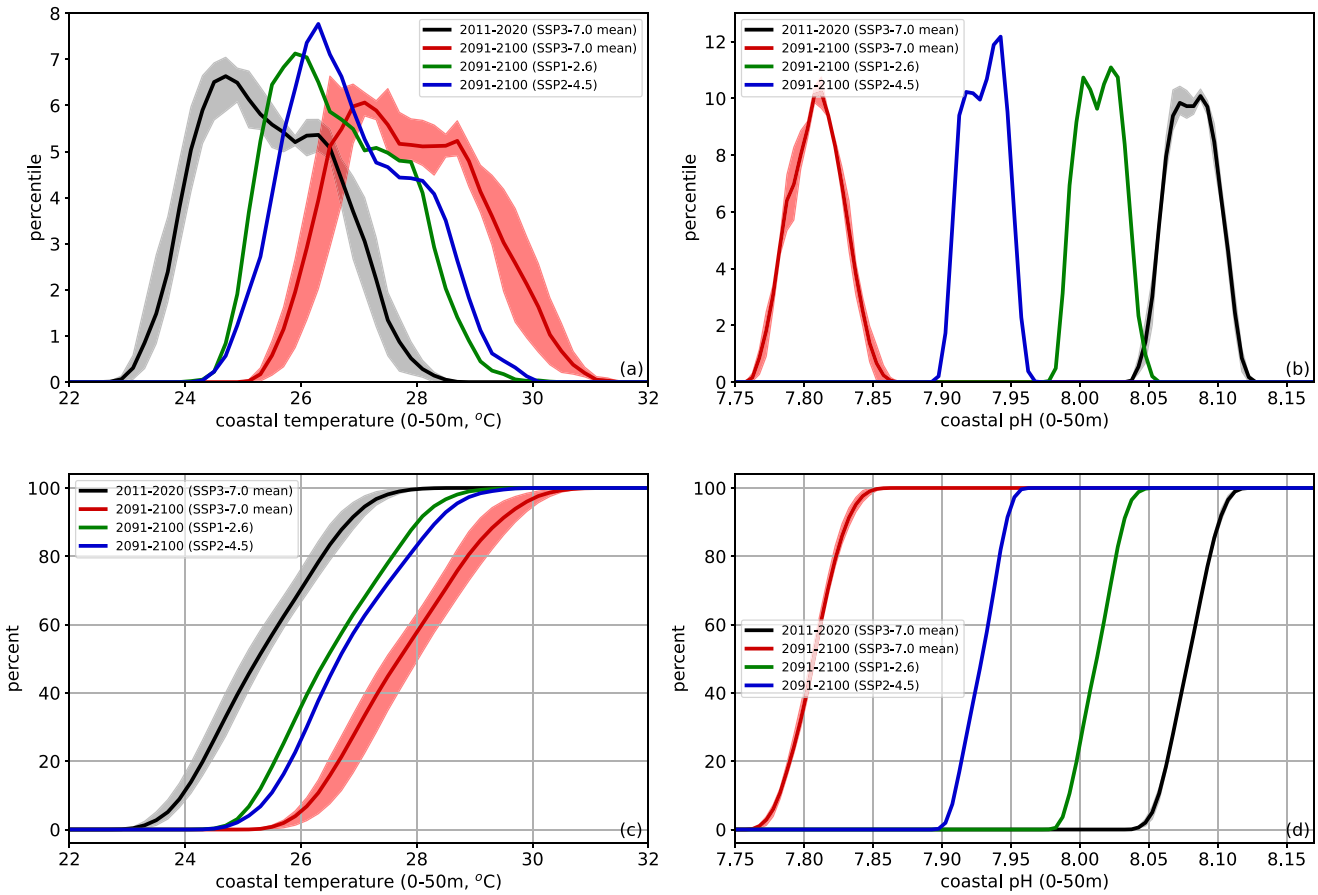

Figure 14. Present-day (2011–2020) and future probability density distributions (PDF; a, b) and cumulative distribution functions (CDF; c, d) of near-surface (0–50 m) coastal temperature (left) and pH (right). SSP3–7.0 (red) and SSP2–4.5 (blue) were averaged for the period 2091–2100. SSP1–2.6 (green) was averaged for the years 2062–2071 which correspond to the period of maximum changes in this scenario. Shading indicates the ensemble spread of the three SSP3–7.0 simulations.

4. Summary and Conclusions

We have presented a methodology to nest a submesoscale permitting model within coarse (∼1° resolution) CESM2 climate projections. This fine-scale regional model—built with ROMS coupled with COBALT—of the MHI is used to downscale three different SSP climate scenarios.

We demonstrate that in order to derive reliable boundary and initial conditions as well as atmospheric forcing for the regional model, the performance of the global model has to be evaluated carefully for the region of interest. If the large-scale signal for the region sufficiently represents the observations, then objective analysis interpolation

Table 4
Overview of 21st Century Changes in Near-Surface (0–50 m) Coastal Temperature and Marine Chemistry Simulated by ROMS/COBALT

	Change in mean (multiples of standard deviation)		
Variable	SSP1–2.6	SSP2–4.5	SSP3–7.0
Temperature (°C)	1.05 (0.97)	1.47 (1.35)	2.44 (2.25)
pH	−0.07 (4.03)	−0.15 (9.10)	−0.27 (16.4)
Aragonite saturation state	−0.32 (4.54)	−0.71 (10.1)	−1.25 (17.8)
Substrate-to-inhibitor ratio ($mol(HCO_3^-)\mu mol(H^+)^{-1}$)	−0.03 (3.74)	−0.06 (7.58)	−0.11 (12.7)

Note. Averages of all three simulations are provided for the SSP3–7.0 scenario. For the SSP1–2.6 scenario maximum changes are given rather than end of century changes.

can be used to map the coarse onto the fine-scales. However, careful detail must be applied to downscaling each and every forcing variable. Some variables can be interpolated directly, while many others require nuanced (bias-correction), statistical (matching variability as in nitrate), or advanced methods (neural-networks) to account for unresolved regional features.

We presented that converting low-resolution CESM2 wind fields into high-resolution wind fields that resolve the wind shear between the islands' mountains and the ocean channels is absolutely essential to represent the MHI near-surface current structure. Furthermore, the removal of biases in salinity, DIC, TA and nutrients simulated by CESM2 results in a substantial improvement of the performance of the regional model as compared to the observations. For overcoming these challenges, the availability of regional long-term observational in situ data such as the Hawaii Ocean Timeseries program and derived mapped data sets such as GLODAP and AVISO as well as local high-resolution atmospheric model output has been indispensable.

Results show that the regional model well represents the known, dominant fine-scale processes of the MHI that CESM2 does not represent while simultaneously maintaining the large-scale structure, temporal variability and trends of the CESM2 model simulations.

Preliminary results of our dynamical downscaling show that the coastal ocean (as well as our entire domain) will be subject to substantial warming regardless of the SSP scenario. Ocean acidification will very likely push near-surface marine carbon chemistry into a completely new and unprecedented state that shares no overlap with present-day conditions.

Data Availability Statement

Simulated and observational data shown in the figures as well as Python Notebooks to generate the figures can be found at: https://osf.io/wzn7g/ (last access: 11 November 2023). Hawaii Ocean Time Series data (HOT, 2023) presented in this study are available through: http://hahana.soest.hawaii.edu/hot/ (last access: 14 February 2024). The complete GLODAPv2 data set (GLODAP, 2023) is available at: https://glodap.info/index.php/mapped-data-product/ (last access: 14 February 2024). AVISO data (AVISO, 2023) used in this study can be accessed at: https://doi.org/10.48670/moi-00148 (last access: 14 February 2024).

Acknowledgments
This research was funded by the National Oceanic and Atmospheric Administration (NOAA) program *MAPP—Modeling Climate Impacts on the Predictability of Fisheries and Other Living Marine Resources* (NA20OAR4310445). T.F. and S.F.G. were supported by the Pacific Islands Ocean Observing System (PacIOOS, http://www.pacioos.hawaii.edu, last access: 15 February 2024), which is a part of the US Integrated Ocean Observing System (IOOS®), funded in part by NOAA Award No. NA16NOS0120024. J.L.G. and K.F. acknowledge the support of the Uehiro Center for the Advancement of Oceanography. G.L. was supported by Office of Naval Research award N00014-21-1-2709. L.H. was supported by NOAA award NA21OAR0170191. The authors would like to thank the Hawaii Ocean Time-series (HOT) project for their continuous efforts to carry out ocean observations around the Hawaiian Islands. We are grateful to the World Climate Research Programme, which, through its Working Group on Coupled Modeling, coordinated and promoted CMIP6. We would also like to thank the climate modeling groups for producing and making available their model output, the Earth System Grid Federation (ESGF) for archiving the data and providing access, as well as the multiple funding agencies who support CMIP6 and ESGF. We thank the CESM2 Large Ensemble Community Project for providing the data for the large-scale projections and acknowledge the supercomputing resources provided by the IBS Center for Climate Physics (ICCP) that made the CESM2 Large Ensemble possible. We would also like to thank three anonymous reviewers and Editor Stephen Griffies for their comments and suggestions that helped improve the manuscript. This is SOEST publication number 11763 and IPRC publication number 1617.

References

Albright, R., Caldeira, L., Hosfelt, J., Kwiatkowski, L., Maclaren, J. K., Mason, B. M., et al. (2016). Reversal of ocean acidification enhances net coral reef calcification. *Nature*, *531*(7594), 362–365. https://doi.org/10.1038/nature17155

Albright, R., Takeshita, Y., Koweek, D. A., Ninokawa, A., Wolfe, K., Rivlin, T., et al. (2018). Carbon dioxide addition to coral reef waters suppresses net community calcification. *Nature*, *555*(7697), 516–519. https://doi.org/10.1038/nature25968

AVISO. (2023). Altimeter satellite gridded sea level anomalies [Dataset]. https://doi.org/10.48670/moi-00148

Bach, L. T. (2015). Reconsidering the role of carbonate ion concentration in calcification by marine organisms. *Biogeosciences*, *12*(16), 4939–4951. https://doi.org/10.5194/bg-12-4939-2015

Bahl, A., Gnanadesikan, A., & Pradal, M.-A. S. (2020). Scaling global warming impacts on ocean ecosystems: Lessons from a suite of Earth system models. *Frontiers in Marine Science*, *7*(698). https://doi.org/10.3389/fmars.2020.00698

Bahr, K. D., Jokiel, P. L., & Rodgers, K. U. S. (2017). Seasonal and annual calcification rates of the Hawaiian reef coral, *Montipora capitata*, under present and future climate change scenarios. *ICES Journal of Marine Science*, *74*(4), 1083–1091. https://doi.org/10.1093/icesjms/fsw078

Bahr, K. D., Rodgers, K. S., & Jokiel, P. L. (2018). Ocean warming drives decline in coral metabolism while acidification highlights species-specific responses. *Marine Biology Research*, *14*(9–10), 924–935. https://doi.org/10.1080/17451000.2018.1551616

Böttjer, D., Dore, J. E., Karl, D. M., Letelier, R. M., Mahaffey, C., Wilson, S. T., et al. (2017). Temporal variability of nitrogen fixation and particulate nitrogen export at Station ALOHA. *Limnology & Oceanography*, *62*(1), 200–216. https://doi.org/10.1002/lno.10386

Bove, C. B., Umbanhowar, J., & Castillo, K. D. (2020). Meta-analysis reveals reduced coral calcification under projected ocean warming but not under acidification across the Caribbean Sea. *Frontiers in Marine Science*, *7*, 127. https://doi.org/10.3389/fmars.2020.00127

Brown, S. L., Landry, M. R., Selph, K. E., Yang, E. J., Rii, Y. M., & Bidigare, R. (2008). Diatoms in the desert: Plankton community response to a mesoscale eddy in the subtropical North Pacific. *Deep Sea Research Part II: Topical Studies in Oceanography*, *55*(10–13), 1321–1333. https://doi.org/10.1016/j.dsr2.2008.02.012

Calil, P. H. R., & Richards, K. J. (2010). Transient upwelling hot spots in the oligotrophic North Pacific. *Journal of Geophysical Research*, *115*(C2), C02003. https://doi.org/10.1029/2009jc005360

Calil, P. H. R., Richards, K. J., Jia, Y., & Bidigare, R. R. (2008). Eddy activity in the lee of the Hawaiian Islands. *Deep Sea Research Part II: Topical Studies in Oceanography*, *55*(10–13), 1179–1194. https://doi.org/10.1016/j.dsr2.2008.01.008

Carter, G. S., Merrifield, M., Becker, J. M., Katsumata, K., Gregg, M., Luther, D., et al. (2008). Energetics of M_2 barotropic-to-baroclinic tidal conversion at the Hawaiian Islands. *Journal of Physical Oceanography*, *38*(10), 2205–2223. https://doi.org/10.1175/2008jpo3860.1

Chan, N. C., & Connolly, S. R. (2013). Sensitivity of coral calcification to ocean acidification: A meta-analysis. *Global Change Biology*, *19*(1), 282–290. https://doi.org/10.1111/gcb.12011

Chavanne, C., Flament, P., Lumpkin, R., Dousset, B., & Bentamy, A. (2002). Scatterometer observations of wind variations induced by oceanic islands: Implications for wind-driven ocean circulation. *Canadian Journal of Remote Sensing*, *28*(3), 466–474. https://doi.org/10.5589/m02-047

Chen, Y. L. (2010). Weather research and forecasting (WRF) regional atmospheric model: Main Hawaiian islands. Distributed by Pacific Islands Ocean Observing System (PacIOOS). Updated 2017. Retrieved from http://pacioos.org/metadata/wrf_hi.html

Church, M. J., Mahaffey, C., Letelier, R. M., Lukas, R., Zehr, J. P., & Karl, D. M. (2009). Physical forcing of nitrogen fixation and diazotroph community structure in the North Pacific subtropical gyre. *Global Biogeochemical Cycles*, *23*(2). https://doi.org/10.1029/2008gb003418

Couespel, D., Levy, M., & Bopp, L. (2021). Oceanic primary production decline halved in eddy-resolving simulations of global warming. *Biogeosciences*, *18*(14), 4321–4349. https://doi.org/10.5194/bg-18-4321-2021

Cyronak, T., Schulz, K. G., & Jokiel, P. L. (2016). The Omega myth: What really drives lower calcification rates in an acidifying ocean. *ICES Journal of Marine Science*, *73*(3), 558–562. https://doi.org/10.1093/icesjms/fsv075

Danabasoglu, G., Lamarque, J.-F., Bacmeister, J., Bailey, D., DuVivier, A., Edwards, J., et al. (2020). The community Earth system model version 2 (CESM2). *Journal of Advances in Modeling Earth Systems*, *12*(2), e2019MS001916. https://doi.org/10.1029/2019ms001916

Dave, A. C., & Lozier, M. S. (2010). Local stratification control of marine productivity in the subtropical North Pacific. *Journal of Geophysical Research*, *115*(C12), C12032. https://doi.org/10.1029/2010jc006507

de Boyer Montégut, C., Madec, G., Fischer, A. S., Lazar, A., & Iudicone, D. (2004). Mixed layer depth over the global ocean: An examination of profile data and a profile-based climatology. *Journal of Geophysical Research*, *109*(C12), C12003. https://doi.org/10.1029/2004jc002378

Dore, J. E., Lukas, R., Sadler, D. W., Church, M. J., & Karl, D. M. (2009). Physical and biogeochemical modulation of ocean acidification in the central North Pacific. *Proceedings of the National Academy of Sciences of the United States of America*, *106*(30), 12235–12240. https://doi.org/10.1073/pnas.0906044106

Drenkard, E. J., Stock, C., Ross, A. C., Dixon, K. W., Adcroft, A., Alexander, M., et al. (2021). Next-generation regional ocean projections for living marine resource management in a changing climate. *ICES Journal of Marine Science*, *78*(6), 1969–1987. https://doi.org/10.1093/icesjms/fsab100

Dushaw, B. D., Howe, B. M., Cornuelle, B. D., Worcester, P. F., & Luther, D. S. (1995). Barotropic and baroclinic tides in the central North Pacific Ocean determined from long-range reciprocal acoustic transmissions. *Journal of Physical Oceanography*, *25*(4), 631–647. https://doi.org/10.1175/1520-0485(1995)025<0631:babtit>2.0.co;2

Egbert, G. D., Bennett, A. F., & Foreman, M. G. G. (1994). TOPEX/POSEIDON tides estimated using a global inverse model. *Journal of Geophysical Research*, *99*(C12), 24821–24852. https://doi.org/10.1029/94JC01894

Eyring, V., Bony, S., Meehl, G. A., Senior, C. A., Stevens, B., Stouffer, R. J., & Taylor, K. E. (2016). Overview of the Coupled Model Intercomparison Project Phase 6 (CMIP6) experimental design and organization. *Geoscientific Model Development*, *9*(5), 1937–1958. https://doi.org/10.5194/gmd-9-1937-2016

Fairall, C. W., Bradley, E. F., Rogers, D. P., Edson, J. B., & Young, G. S. (1996). Bulk parameterization of air-sea fluxes for tropical ocean–global atmosphere coupled-ocean atmosphere response experiment. *Journal of Geophysical Research*, *101*(C2), 3747–3764. https://doi.org/10.1029/95JC03205

Friedrich, T., Powell, B., Stock, C., Hahn-Woernle, L., Dussin, R., & Curchitser, E. (2021). Drivers of phytoplankton blooms in Hawaii: A regional model study. *Journal of Geophysical Research: Oceans*, *126*(5), e2020JC017069. https://doi.org/10.1029/2020jc017069

Frölicher, T. L., Fischer, E. M., & Gruber, N. (2018). Marine heatwaves under global warming. *Nature*, *560*(7718), 360–364. https://doi.org/10.1038/s41586-018-0383-9

Frölicher, T. L., Rodgers, K. B., Stock, C. A., & Cheung, W. W. (2016). Sources of uncertainties in 21st century projections of potential ocean ecosystem stressors. *Global Biogeochemical Cycles*, *30*(8), 1224–1243. https://doi.org/10.1002/2015gb005338

Glantz, M. H., & Ramirez, I. J. (2020). Reviewing the Oceanic Niño Index (ONI) to enhance societal readiness for El Niño's impacts. *International Journal of Disaster Risk Science*, *11*(3), 394–403. https://doi.org/10.1007/s13753-020-00275-w

GLODAP. (2023). Global ocean data analysis project version 2 [Dataset]. https://doi.org/10.5194/essd-14-5543-2022

Glynn, P., & D'croz, L. (1990). Experimental evidence for high temperature stress as the cause of El Niño-coincident coral mortality. *Coral Reefs*, *8*(4), 181–191. https://doi.org/10.1007/bf00265009

Gove, J. M., McManus, M. A., Neuheimer, A. B., Polovina, J. J., Drazen, J. C., Smith, C. R., et al. (2016). Near-island biological hotspots in barren ocean basins. *Nature Communications*, *7*(1), 1–8. https://doi.org/10.1038/ncomms10581

Gruber, N., Hauri, C., Lachkar, Z., Loher, D., Frölicher, T. L., & Plattner, G.-K. (2012). Rapid progression of ocean acidification in the California Current System. *Science*, *337*(6091), 220–223. https://doi.org/10.1126/science.1216773

Hauri, C., Gruber, N., McDonnell, A., & Vogt, M. (2013). The intensity, duration, and severity of low aragonite saturation state events on the California continental shelf. *Geophysical Research Letters*, *40*(13), 3424–3428. https://doi.org/10.1002/grl.50618

Hersbach, H., Bell, B., Berrisford, P., Hirahara, S., Horányi, A., Muñoz-Sabater, J., et al. (2020). The ERA5 global reanalysis. *Quarterly Journal of the Royal Meteorological Society*, *146*(730), 1999–2049. https://doi.org/10.1002/qj.3803

Hitzl, D. E., Chen, Y.-L., & Hsiao, F. (2020). Wintertime easterly and southeasterly airflow in the 'Alenuihaha Channel. *Monthly Weather Review*, *148*(4), 1337–1362. https://doi.org/10.1175/mwr-d-19-0042.1

Hitzl, D. E., Chen, Y.-L., & Van Nguyen, H. (2014). Numerical simulations and observations of airflow through the 'Alenuihāhā Channel, Hawaii. *Monthly Weather Review*, *142*(12), 4696–4718. https://doi.org/10.1175/mwr-d-13-00312.1

HMRG. (2017). Hawaii mapping research group [Dataset]. University of Hawaii. Retrieved from http://www.soest.hawaii.edu/HMRG/multibeam/index.php

Höhlein, K., Kern, M., Hewson, T., & Westermann, R. (2020). A comparative study of convolutional neural network models for wind field downscaling. *Meteorological Applications*, *27*(6), e1961. https://doi.org/10.1002/met.1961

Holdsworth, A. M., Zhai, L., Lu, Y., & Christian, J. R. (2021). Future changes in oceanography and biogeochemistry along the Canadian Pacific continental margin. *Frontiers in Marine Science*, *8*, 602991. https://doi.org/10.3389/fmars.2021.602991

HOT. (2023). Hawaii ocean time-series data organization & graphical systems (HOT-DOGS) [Dataset]. Retrieved from https://hahana.soest.hawaii.edu/hot/hot-dogs/interface.html

Hu, S., Sprintall, J., Guan, C., Hu, D., Wang, F., Lu, X., & Li, S. (2020). Observed triple mode of salinity variability in the thermocline of tropical Pacific Ocean. *Journal of Geophysical Research: Oceans*, *125*(9), e2020JC016210. https://doi.org/10.1029/2020jc016210

Huang, B., Thorne, P. W., Banzon, V. F., Boyer, T., Chepurin, G., Lawrimore, J. H., et al. (2017). Extended reconstructed sea surface temperature, version 5 (ERSSTv5): Upgrades, validations, and intercomparisons. *Journal of Climate*, *30*(20), 8179–8205. https://doi.org/10.1175/jcli-d-16-0836.1

Jan, S., & Chen, C.-T. A. (2009). Potential biogeochemical effects from vigorous internal tides generated in Luzon Strait: A case study at the southernmost coast of Taiwan. *Journal of Geophysical Research*, *114*(C4), C04021. https://doi.org/10.1029/2008jc004887

Karl, D. M., & Church, M. J. (2017). Ecosystem structure and dynamics in the North Pacific Subtropical Gyre: New views of an old ocean. *Ecosystems*, *20*(3), 433–457. https://doi.org/10.1007/s10021-017-0117-0

Karl, D. M., & Church, M. J. (2018). Station ALOHA: A gathering place for discovery, education, and scientific collaboration. *Limnology and Oceanography Bulletin*, *28*(1), 10–12. https://doi.org/10.1002/lob.10285

Karl, D. M., & Lukas, R. (1996). The Hawaii Ocean Time-series (HOT) program: Background, rationale and field implementation. *Deep Sea Research Part II: Topical Studies in Oceanography*, *43*(2–3), 129–156. https://doi.org/10.1016/0967-0645(96)00005-7

Kleypas, J. A., Buddemeier, R. W., Archer, D., Gattuso, J.-P., Langdon, C., & Opdyke, B. N. (1999). Geochemical consequences of increased atmospheric carbon dioxide on coral reefs. *Science*, *284*(5411), 118–120. https://doi.org/10.1126/science.284.5411.118

Kwiatkowski, L., Torres, O., Bopp, L., Aumont, O., Chamberlain, M., Christian, J. R., et al. (2020). Twenty-first century ocean warming, acidification, deoxygenation, and upper-ocean nutrient and primary production decline from CMIP6 model projections. *Biogeosciences*, *17*(13), 3439–3470. https://doi.org/10.5194/bg-17-3439-2020

Langdon, C., & Atkinson, M. (2005). Effect of elevated pCO_2 on photosynthesis and calcification of corals and interactions with seasonal change in temperature/irradiance and nutrient enrichment. *Journal of Geophysical Research*, *110*(C9), C09S07. https://doi.org/10.1029/2004jc002576

Lauvset, S. K., Key, R. M., Olsen, A., Van Heuven, S., Velo, A., Lin, X., et al. (2016). A new global interior ocean mapped climatology: The 1×1 GLODAP version 2. *Earth System Science Data*, *8*(2), 325–340. https://doi.org/10.5194/essd-8-325-2016

Leitner, A. B., Friedrich, T., Kelley, C. D., Travis, S., Partridge, D., Powell, B., & Drazen, J. C. (2021). Biogeophysical influence of large-scale bathymetric habitat types on mesophotic and upper bathyal demersal fish assemblages: A Hawaiian case study. *Marine Ecology Progress Series*, *659*, 219–236. https://doi.org/10.3354/meps13581

Letelier, R. M., Björkman, K. M., Church, M. J., Hamilton, D. S., Mahowald, N. M., Scanza, R. A., et al. (2019). Climate-driven oscillation of phosphorus and iron limitation in the North Pacific subtropical gyre. *Proceedings of the National Academy of Sciences of the United States of America*, *116*(26), 12720–12728. https://doi.org/10.1073/pnas.1900789116

Lévy, M., Franks, P. J., & Smith, K. S. (2018). The role of submesoscale currents in structuring marine ecosystems. *Nature Communications*, *9*(4758), 4758. https://doi.org/10.1038/s41467-018-07059-3

Liu, G., Powell, B., & Friedrich, T. (2023). Climate downscaling for regional models with a neural network: A Hawaiian example. *Progress in Oceanography*, *215*, 103047. https://doi.org/10.1016/j.pocean.2023.103047

Long, M. C., Moore, J. K., Lindsay, K., Levy, M., Doney, S. C., Luo, J. Y., et al. (2021). Simulations with the marine biogeochemistry library (MARBL). *Journal of Advances in Modeling Earth Systems*, *13*(12), e2021MS002647. https://doi.org/10.1029/2021ms002647

Lukas, R. (2001). Freshening of the upper thermocline in the North Pacific subtropical gyre associated with decadal changes of rainfall. *Geophysical Research Letters*, *28*(18), 3485–3488. https://doi.org/10.1029/2001gl013116

Lumpkin, R., & Flament, P. (2013). Extent and energetics of the Hawaiian Lee Countercurrent. *Oceanography*, *26*(1), 58–65. https://doi.org/10.5670/oceanog.2013.05

Macías, D., Martin, A., García-Lafuente, J., García, C., Yool, A., Bruno, M., et al. (2007). Analysis of mixing and biogeochemical effects induced by tides on the Atlantic–Mediterranean flow in the Strait of Gibraltar through a physical–biological coupled model. *Progress in Oceanography*, *74*(2–3), 252–272. https://doi.org/10.1016/j.pocean.2007.04.006

Mahadevan, A. (2016). The impact of submesoscale physics on primary productivity of plankton. *Annual Review of Marine Science*, *8*(1), 161–184. https://doi.org/10.1146/annurev-marine-010814-015912

Maher, N., Wills, R. C. J., DiNezio, P., Klavans, J., Milinski, S., Sanchez, S. C., et al. (2022). The future of the El Niño-southern oscillation: Using large ensembles to illuminate time-varying responses and inter-model differences. *Earth System Dynamics Discussions*, 1–28.

Manizza, M., Le Quéré, C., Watson, A. J., & Buitenhuis, E. T. (2005). Bio-optical feedbacks among phytoplankton, upper ocean physics and sea-ice in a global model. *Geophysical Research Letters*, *32*(5), L05603. https://doi.org/10.1029/2004GL020778

McGillicuddy, D. J., Jr. (2016). Mechanisms of physical-biological-biogeochemical interaction at the oceanic mesoscale. *Annual Review of Marine Science*, *8*(1), 125–159. https://doi.org/10.1146/annurev-marine-010814-015606

McIntosh, P. C. (1990). Oceanographic data interpolation: Objective analysis and splines. *Journal of Geophysical Research*, *95*(C8), 13529–-13541. https://doi.org/10.1029/JC095iC08p13529

Nencioli, F., Kuwahara, V. S., Dickey, T. D., Rii, Y. M., & Bidigare, R. R. (2008). Physical dynamics and biological implications of a mesoscale eddy in the lee of Hawai'i: Cyclone Opal observations during E-Flux III. *Deep Sea Research Part II: Topical Studies in Oceanography*, *55*(10–13), 1252–1274. https://doi.org/10.1016/j.dsr2.2008.02.003

O'Neill, B. C., Tebaldi, C., Van Vuuren, D. P., Eyring, V., Friedlingstein, P., Hurtt, G., et al. (2016). The scenario model intercomparison project (ScenarioMIP) for CMIP6. *Geoscientific Model Development*, *9*(9), 3461–3482. https://doi.org/10.5194/gmd-9-3461-2016

Orr, J. C., Fabry, V. J., Aumont, O., Bopp, L., Doney, S. C., Feely, R. A., et al. (2005). Anthropogenic ocean acidification over the twenty-first century and its impact on calcifying organisms. *Nature*, *437*(7059), 681–686. https://doi.org/10.1038/nature04095

Partridge, D., Friedrich, T., & Powell, B. S. (2019). Reanalysis of the PacIOOS Hawaiian Island ocean forecast system, an implementation of the regional ocean modeling system v3. 6. *Geoscientific Model Development*, *12*(1), 195–213. https://doi.org/10.5194/gmd-12-195-2019

Pilcher, D. J., Cross, J. N., Hermann, A. J., Kearney, K. A., Cheng, W., & Mathis, J. T. (2022). Dynamically downscaled projections of ocean acidification for the Bering Sea. *Deep Sea Research Part II: Topical Studies in Oceanography*, *198*, 105055. https://doi.org/10.1016/j.dsr2.2022.105055

Powell, B., Janeković, I., Carter, G., & Merrifield, M. (2012). Sensitivity of internal tide generation in Hawaii. *Geophysical Research Letters*, *39*(10), L10606. https://doi.org/10.1029/2012gl051724

Qiu, B., & Chen, S. (2010). Interannual variability of the North Pacific subtropical countercurrent and its associated mesoscale eddy field. *Journal of Physical Oceanography*, *40*(1), 213–225. https://doi.org/10.1175/2009jpo4285.1

Qiu, B., & Durland, T. S. (2002). Interaction between an island and the ventilated thermocline: Implications for the Hawaiian Lee Countercurrent. *Journal of Physical Oceanography*, *32*(12), 3408–3426. https://doi.org/10.1175/1520-0485(2002)032<3408:ibaiat>2.0.co;2

Qiu, B., Rudnick, D. L., Chen, S., & Kashino, Y. (2013). Quasi-stationary north equatorial undercurrent jets across the tropical North Pacific Ocean. *Geophysical Research Letters*, *40*(10), 2183–2187. https://doi.org/10.1002/grl.50394

Ray, R. D., & Mitchum, G. T. (1996). Surface manifestation of internal tides generated near Hawai'i. *Geophysical Research Letters*, *23*(16), 2101–2104. https://doi.org/10.1029/96gl02050

Ray, R. D., & Mitchum, G. T. (1997). Surface manifestation of internal tides in the deep ocean: Observations from altimetry and island gauges. *Progress in Oceanography*, *40*(1–4), 135–162. https://doi.org/10.1016/s0079-6611(97)00025-6

Redfield, A. C. (1963). The influence of organisms on the composition of seawater. *The Sea*, *2*, 26–77.

Rii, Y. M., Brown, S. L., Nencioli, F., Kuwahara, V., Dickey, T., Karl, D. M., & Bidigare, R. R. (2008). The transient oasis: Nutrient-phytoplankton dynamics and particle export in Hawaiian lee cyclones. *Deep Sea Research Part II: Topical Studies in Oceanography*, *55*(10–13), 1275–1290. https://doi.org/10.1016/j.dsr2.2008.01.013

Rodgers, K. B., Lee, S.-S., Rosenbloom, N., Timmermann, A., Danabasoglu, G., Deser, C., et al. (2021). Ubiquity of human-induced changes in climate variability. *Earth System Dynamics*, *12*(4), 1393–1411. https://doi.org/10.5194/esd-12-1393-2021

Shchepetkin, A. F., & McWilliams, J. C. (1998). Quasi-monotone advection schemes based on explicit locally adaptive dissipation. *Monthly Weather Review*, *126*(6), 1541–1580. https://doi.org/10.1175/1520-0493(1998)126⟨1541:QMASBO⟩2.0.CO;2

Shchepetkin, A. F., & McWilliams, J. C. (2003). A method for computing horizontal pressure-gradient force in an oceanic model with a nonaligned vertical coordinate. *Journal of Geophysical Research*, *108*(C3), 3090. https://doi.org/10.1029/2001JC001047

Shchepetkin, A. F., & McWilliams, J. C. (2005). The regional oceanic modeling system (ROMS): A split-explicit, free-surface, topography-following-coordinate oceanic model. *Ocean Modelling*, *9*(4), 347–404. https://doi.org/10.1016/j.ocemod.2004.08.002

Siedlecki, S. A., Salisbury, J., Gledhill, D., Bastidas, C., Meseck, S., McGarry, K., et al. (2021). Projecting ocean acidification impacts for the Gulf of Maine to 2050: New tools and expectations. *Elementa: Science of the Anthropocene*, *9*(1), 00062. https://doi.org/10.1525/elementa.2020.00062

Siedlecki, S. A., Pilcher, D., Howard, E. M., Deutsch, C., MacCready, P., Norton, E. L., et al. (2021). Coastal processes modify projections of some climate-driven stressors in the California Current System. *Biogeosciences*, *18*(9), 2871–2890. https://doi.org/10.5194/bg-18-2871-2021

Souza, J. M. A. C., Powell, B. S., Castillo-Trujillo, A. C., & Flament, P. (2015). The vorticity balance of the ocean surface in Hawaii from a regional reanalysis. *Journal of Physical Oceanography*, *45*(2), 424–440. https://doi.org/10.1175/JPO-D-14-0074.1

Stock, C. A., Dunne, J. P., & John, J. G. (2014). Global-scale carbon and energy flows through the marine planktonic food web: An analysis with a coupled physical–biological model. *Progress in Oceanography*, *120*, 1–28. https://doi.org/10.1016/j.pocean.2013.07.001

Stopa, J. E., Filipot, J.-F., Li, N., Cheung, K. F., Chen, Y.-L., & Vega, L. (2013). Wave energy resources along the Hawaiian Island chain. *Renewable Energy*, *55*, 305–321. https://doi.org/10.1016/j.renene.2012.12.030

Tu, C.-C., Chen, Y.-L., Chen, S.-Y., Kuo, Y.-H., & Lin, P.-L. (2017). Impacts of including rain evaporative cooling in the initial conditions on the prediction of a coastal heavy rainfall event during TiMREX. *Monthly Weather Review*, *145*(1), 253–277. https://doi.org/10.1175/mwr-d-16-0224.1

Webb, E. J., & Magi, B. I. (2022). The ensemble oceanic Niño index. *International Journal of Climatology*, *42*(10), 5321–5341. https://doi.org/10.1002/joc.7535

Wong-Ala, J. A., Comfort, C. M., Gove, J. M., Hixon, M. A., McManus, M. A., Powell, B. S., et al. (2018). How life history characteristics and environmental forcing shape settlement success of coral reef fishes. *Frontiers in Marine Science*, *5*, 65. https://doi.org/10.3389/fmars.2018.00065

Xie, S.-P., Liu, W. T., Liu, Q., & Nonaka, M. (2001). Far-reaching effects of the Hawaiian Islands on the Pacific ocean-atmosphere system. *Science*, *292*(5524), 2057–2060. https://doi.org/10.1126/science.1059781

Yoshida, S., Qiu, B., & Hacker, P. (2010). Wind-generated eddy characteristics in the lee of the island of Hawaii. *Journal of Geophysical Research*, *115*(C3), C03019. https://doi.org/10.1029/2009jc005417

Yu, J.-Y., Zou, Y., Kim, S. T., & Lee, T. (2012). The changing impact of El Niño on US winter temperatures. *Geophysical Research Letters*, *39*(15), L15702. https://doi.org/10.1029/2012gl052483

Zho, C., & Chen, Y.-L. (2014). Assimilation of GPS RO refractivity data and its impact on simulations of trade wind inversion and a winter cold front in Hawaii. *Natural Science*, *6*(08), 605–614. https://doi.org/10.4236/ns.2014.68060